Mixed Bayesian Network for reliability assessment of RC structures subjected to environmental actions

Hongyuan Guo, You Dong, Emilio Bastidas-Arteaga

Please cite this paper as:
Guo, H., Dong, Y., Bastidas-Arteaga, E. (2024). Mixed Bayesian Network for reliability assessment of RC structures subjected to environmental actions. Structural Safety, 106, 102392. https://doi.org/10.1016/j.strusafe.2023.102392

Mixed Bayesian Network for reliability assessment of RC structures subject to environmental actions

Hongyuan Guo[1], You Dong[1,*], and Emilio Bastidas-Arteaga[2]

1. Department of Civil and Environmental Engineering, The Hong Kong Polytechnic University, Hong Kong, China

2. La Rochelle University, LaSIE UMR CNRS 7356, La Rochelle, France

Abstract: Under environmental action, reinforced concrete (RC) structures might suffer from reinforcement corrosion caused by the surrounding environment, dramatically reducing structural reliability and threatening social development. However, most of the existing reliability assessment methods for RC structures only focused on the structural performance at the design stage given the original unchanged environment, ignoring the effects of realistic exposure conditions and inspection results on reliability evaluation. Thus, this paper develops a general reliability assessment framework based on a Mixed Bayesian network (MBN), incorporating three modules, i.e., durability assessment, load-bearing capacity analysis, and time-dependent reliability analysis. In MBN, separate sub-BNs are built based on different modules and connected by pinch point variables where probabilistic information is transmitted via soft evidence. Besides, this framework considers time-dependent environmental parameters and two-dimensional chloride transport and their effects on reliability. Meanwhile, adjustment coefficients are applied to improve the results of the analytical mechanical model with respect to different limit states through the finite element model (FEM). The proposed MBN framework is illustrated for a corroded RC beam under a marine atmospheric environment to investigate the effects of environmental modeling, chloride transport patterns, and concrete crack inspection on reliability assessment. The results indicate that under the assumed conditions in the case study, early inspection of large cracks may significantly overestimate the failure probability by about 500%. Besides, failure probability might be underestimated by about 95%, ignoring the time-variant environment and two-dimensional chloride transport.

Keywords: Bayesian Network; Reliability Assessment; Reinforced Concrete; Environmental Actions; Reinforcement Corrosion

[**] **Corresponding Author**
E-mail address: you.dong@polyu.edu.hk
Tel.: +852-3400 8818

1. Introduction

During the service life of reinforced concrete (RC) structures, their mechanical performances deteriorate over time due to long-term environmental impacts (e.g., chloride ingress and concrete carbonation etc.) [1–3]. According to ASCE 2021 report card for America's infrastructure [4], there are 46,154 bridges representing 7.5% of the overall bridges in the USA, with structural deficiencies. The costs for overcoming the detrimental impacts of structural deficiencies are enormous and intractable. In 2022, a study by the financial accountability office of Ontario estimated that $10.1 billion should be annually spent to keep a safe state in the existing local portfolio of public buildings and facilities [5]. Therefore, this deterioration of structural performance could produce severe direct and indirect social impacts – e.g., delays, unavailability of structure assets, etc.

Various studies indicated that RC structural performance is mainly caused by chloride or carbonation-induced reinforcement corrosion [3,6]. Consequently, many efforts have been made to assess the reliability of corroded RC structures over time. In 1997, Frangopol *et al.* [7] proposed a reliability assessment method for RC girders subject to chloride ingress and implemented reliability-based life-cycle cost evaluation. Furthermore, considering the pitting corrosion and its spatial effects on RC structures, Stewart and his collaborators [8–11] conducted a series of research relating to Monte Carlo simulation (MCS) based reliability analysis. Similarly, Val [12] investigated the time-dependent reliability of corroded RC beams subject to different failure modes, including flexural and shear failure. Guo *et al.* [13] developed a two-step translation method to perform the time-dependent reliability analysis for corroded RC structures efficiently. However, these studies focused on a fixed environment, while realistic environmental conditions combine time dependency, nonlinearity, and uncertainty. Therefore, Bastidas-Arteaga *et al.* [14] proposed a reliability assessment method for RC structures with respect to the effects of carbon emissions-induced climate change on structural performance. In addition, the existing studies associated with the reliability assessment of RC structures usually applied analytical models and lacked experimental validation [15]. Thus, Zhang *et al*. [16] used Finite Element Modeling (FEM) and X-ray photographs integrated with experimental validation and MCS to achieve the reliability analysis of corroded RC beams. Guo *et al.* [17] also employed experimental validation, FEM, and polynomial chaos expansions to develop a general framework of global sensitivity and probabilistic analysis for failure analysis of corroded RC structures. However, these studies focused on their reliability assessment at the design stage, which ignores actual exposure conditions and inspection results, and might misestimate the capacity and reliability of RC structures. Therefore, it is still necessary to consider the above-mentioned aspects to improve the reliability assessment/updating of RC structures.

Bayesian methods have been commonly utilized to perform probabilistic inference by updating the data collected from monitoring systems or in-situ inspections [18]. Since many parameters (environmental, material, etc.) are involved in practical engineering systems, it might be challenging to use traditional Bayesian methods for parameter updating and inference. To this end, a graphical model called Bayesian Network (BN) has been widely applied to update the reliability assessment of RC structures through probabilistic inspection data [19,20]. For instance, considering carbonation-induced reinforcement corrosion,

Tesfamariam and Martín-Pérez [21] built a BN model to investigate the effects of exposure conditions on the carbonation rate and the corrosion probability. Deby *et al.* [22,23] applied BN to implement reliability analysis for RC structures subject to chloride ingress. Tran *et al.* [24–26] conducted a series of studies to identify the uncertainties of parameters and corrosion initiation probability for deteriorating RC structures under chloride ingress. However, those studies usually adopted static Bayesian Networks (SBN), which did not consider the time-dependency of some parameters involved in the problem – e.g., concrete aging, surface chloride concentration, loading, etc. Therefore, to handle BN updating and inferences under multiple time slices, Dynamic Bayesian Network (DBN) has been proposed [27,28]. For instance, Guo and Dong [2] developed a general DBN framework for the durability assessment of RC structures with respect to the marine atmospheric environment. Considering the uncertainties in climate change and chloride transport, such a framework could investigate the effects of inspected concrete cracks on the durability of RC structures. However, such a DBN framework only concerns the durability assessment of RC structures rather than their mechanical properties. Therefore, the study cannot be directly applied to the time-dependent reliability assessment of RC structures under environmental actions when focusing on ultimate limit states.

In order to perform a BN-based life-cycle reliability analysis for corroded RC structures, it is imperative to consider the effects of environmental-induced reinforcement corrosion on the performance of RC structures. For example, Ma *et al.* [29] established a BN integrating with in-situ loading tests to predict the performance deterioration and structural response of existing corroded RC bridges. However, due to the absence of DBN, this study might be inappropriate for the time-dependent reliability analysis of RC structures. Thus, Hackl and Kohler [30] proposed a DBN framework for the reliability assessment of corroded RC structures subject to chloride transport by integrating parameters associated with the deterioration process. Although this study considers time dependencies using DBN, many issues still need to be addressed. For instance, such an existing DBN framework did not consider climate change and applied a simplified one-dimensional Fick's law for chloride transport prediction, which might lead to errors on the durability performance and reliability assessments under realistic exposure conditions and two-dimensional chloride ingress (RC beams and columns) [1,31,32]. In addition, the existing DBN framework still adopted analytical mechanical models and ignored the corrosion-induced spatial effects, which might misestimate the mechanical performance and reliability level of RC structures. These issues could be solved by considering comprehensive deterioration models such as those in [14,17,33]. However, the computational cost for the BN modeling and inference would grow exponentially for this type of model that requires several input parameters [19,20]. Therefore, there is still a need to propose a novel BN framework for RC structural reliability assessment/updating, doing a trade-off between model complexity and efficiency.

This study proposes a comprehensive BN framework for the life-cycle reliability assessment of RC structures under the marine atmospheric environment. The framework incorporates several physical models for the durability and reliability assessment/updating of RC structures, including a two-dimensional chloride transport model and analytical and finite element methods for RC structural performance analysis (Section 3). In order to reduce the

difficulty in BN modeling involving many parameters, this paper establishes a new Mixed Bayesian Network (MBN) (Section 4). Finally, the proposed MBN framework is illustrated with a time-dependent reliability analysis of RC beams placed in a marine atmospheric environment. In this case study, we examine the effects of environmental models, patterns of chloride transport, and inspection results on reliability assessment/updating.

2. Principal concepts of the proposed framework

As illustrated in Fig. 1, the proposed framework for the reliability assessment of RC structures subject to marine atmospheric environment comprises three main stages: durability assessment, mechanical evaluation, and reliability assessment. In the first stage, the boundary conditions of the structure (external temperature, relative humidity, and chloride concentration) are obtained via environmental modeling. A chloride transport model is used to determine the corrosion initiation time. When corrosion initiates, the corrosion rate i_{corr} and the radius reduction of reinforcement Δr could be evaluated. The numerical model for this first stage has been developed in a previous study [2]. The main results of stage 1 (i_{corr} and Δr) are transferred to the next stage (mechanical evaluation) to assess flexural and shear capacity (P_{Mu} and P_{Vu}) and to carry out FEM analysis. In the last stage, reliability assessment and failure mode analysis are performed in terms of the results of the mechanical assessment in the second stage. The mechanical evaluation and reliability computation models are detailed in Section 3.

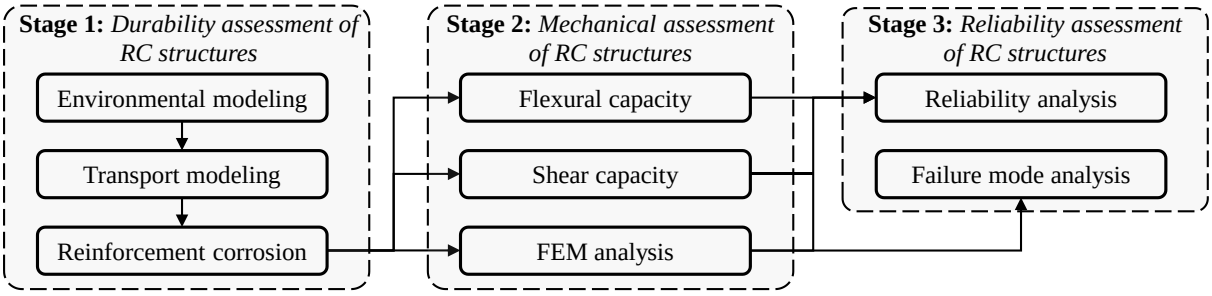

Fig. 1 Modular reliability assessment framework for corroding RC structures

The direct implementation of the proposed framework using traditional Bayesian Networks (BNs) poses significant computational challenges [2,30,34]. Firstly, the large number of time-slices or links and nodes in the network requires substantial physical memory to store critical information, such as conditional probability tables (CPTs), resulting in longer computation times for probabilistic inference. Secondly, to achieve accurate inference, all continuous nodes must be discretized into discrete nodes, leading to exponential growth in physical memory requirements as the number of discrete node states increases. Lastly, constructing a comprehensive DBN demands a large number of data samples to generate precise node CPTs for subsequent probabilistic inference tasks.

To address these challenges, this study proposes a novel approach called Multiple Bayesian Networks (MBN). In this study, MBN is constructed and updated at each stage by integrating diverse models and analysis methods, with the pinch-point variables (i_{corr}, Δr, P_{Mu}, and P_{Vu}) serving as bridges between the different sub-BNs. This innovative MBN method is detailed in Section 4, providing an effective solution to handle the complexities of

information updating and probabilistic inference without resorting to a large and complex BN.

3. Performance assessment models of RC structures

3.1.Durability assessment of RC structures

In this section, the basic models employed in the durability assessment, including environmental modeling, chloride transport prediction, and corrosion degree and concrete crack evaluations, are briefly reviewed from previous studies [2,35]. Due to limited experimental and theoretical studies on the spatial correlation of other parameters (i.e., chloride diffusion coefficients and rebar corrosion rates) [36,37], the effect of spatial correlation on durability assessment is not directly considered in this section. Instead, the corrosion non-uniformity factor R is adopted to indirectly address the issues related to spatial correlation (Section 3.2) [2,13,38].

3.1.1. Environmental modeling and chloride ingress

Realistic modeling of environmental parameters, e.g., temperature, relative humidity (RH), and chloride deposition, is essential for the durability assessment of RC structures. Therefore, an environmental model is employed to account for various factors, including the characteristic value of exposure conditions *ec* (representing the average temperature rise from 1970 to 2090 [39]), the seasonal variations $f_{\text{sea}}(t)$ and daily variations $f_{\text{dai}}(t)$, an increasing tendency f_{inc}, and a white noise ξ. These factors are described by Eqs.(1)-(4) [1,39]. Given the parameters in Eqs.(1)-(4) and *ec*, temperature, relative humidity (RH), and chloride deposition at any time instant could be calculated.

$$f(ec,t) = f_{\text{sea}}(t) + f_{\text{dai}}(t) + f_{\text{inc}}(ec,t) + \xi \tag{1}$$

$$f_{\text{sea}}(t) = a_1 \cdot \sin\left[w_1 (t - t_{\text{ref}}) \big/ 365 + b_1\right] + a_2 \cdot \sin\left[2 w_1 (t - t_{\text{ref}}) \big/ 365 + b_2\right] + a_0 \tag{2}$$

$$f_{\text{dai}}(t) = a_{01} - a_{11}\cos(w_{11}t) + b_{11}\sin(w_{11}t) - a_{21}\cos(2w_{11}t) - b_{21}\sin(2w_{11}t) \tag{3}$$

$$f_{\text{inc}}(ec,t) = \left(5.04\times10^{-3}ec^2 - 3.57\times10^{-2}ec + 6.49\times10^{-2}\right)\cdot\left[(t - t_{\text{ref}})/365\right]^{0.359ec+0.333} \tag{4}$$

where t and t_{ref} are current and reference time (day); a_0 is the baseline average mean annual value; a_1, a_2, b_1, b_2, w_1, and w_2 are the parameters of $f_{\text{sea}}(t)$; and a_{01}, a_{11}, a_{21}, b_{11}, b_{21} and w_{11} are the parameters of $f_{\text{dai}}(t)$. In section 5, an example of this model is presented.

Existing studies have consistently shown that chloride ingression is the primary threat to RC structures exposed to marine atmospheric environments [38,40]. Consequently, chloride ingression is specifically considered in this study. Given the boundary conditions provided by Eqs.(1)-(4), the chloride ingress process into concrete could be simulated by the following three steps [1]:

(1) Solve the heat transfer equation, i.e., Eq. (5) [41]

$$\rho_c \cdot c_q \frac{\partial T}{\partial t} = \lambda \nabla T = \lambda\left(\frac{\partial^2 T}{\partial x^2} + \frac{\partial^2 T}{\partial y^2}\right) \tag{5}$$

where T is the current temperature (K); x and y are the horizontal and vertical coordinates (m)

of cross-sections; ρ_c, c_q, and λ are denoted as concrete density, heat capacity, and thermal conductivity, respectively.

(2) Solve the moisture diffusion equation, i.e., Eq. (6) [31];

$$\frac{\partial w_e}{\partial h_{RH}} \frac{\partial h_{RH}}{\partial t} = D_h \left(\frac{\partial h_{RH}}{\partial x^2} + \frac{\partial h_{RH}}{\partial y^2} \right) \tag{6}$$

where h_{RH} is the relative humidity (RH) inside the concrete, and D_h is the coefficient of humidity diffusion (m^2/s) related to T, t, and RH [42].

(3) Solve the chloride transport equation, i.e., Eq. (7) [31].

$$\frac{\partial C_{fc}}{\partial t} = D_c^* \left(\frac{\partial^2 C_{fc}}{\partial x^2} + \frac{\partial^2 C_{fc}}{\partial y^2} \right) + D_h^* \left(\frac{\partial}{\partial x} \left(C_{fc} \frac{\partial h_{RH}}{\partial x} \right) + \frac{\partial}{\partial y} \left(C_{fc} \frac{\partial h_{RH}}{\partial y} \right) \right) \tag{7}$$

where C_{fc} is free chloride content (kg/m^3 of pore solution); and D_c^* and D_h^* are the apparent diffusion coefficients of chlorides and moisture (m^2/s), respectively. The alternating-direction implicit-based finite difference method is employed to solve Eqs. (5)-(7) [43] due to its high nonlinearity and two-dimensional formulation.

3.1.2. Reinforcement corrosion and concrete cracking

The simulation of chloride transport in Section 3.1.1 provides the chloride content on the reinforcement surface c_{bar}. The reinforcement corrosion would start once c_{bar} is beyond critical value c_{cr}. After corrosion initiation, the corrosion rate of reinforcement is evaluated by Liu's model [44]:

$$\begin{aligned} \ln\left[1.08 i_{corr}(t)\right] &= 7.89 + 0.7771 \cdot \ln(1.69 c_{bar}) \\ &- 3006/T_{con} - 0.000116 \cdot R_{con} + 2.24 t_{corr}^{-0.215} + \vartheta \end{aligned} \tag{8}$$

where $i_{corr}(t)$ is the corrosion current density ($\mu A/cm^2$); T_{con} and R_{con} (Ohms) are the temperature and resistance within the concrete; t_{corr} (year) is the time after corrosion initiation; and ϑ denotes a white noise following $N(0, 0.3312)$ [39].

According to Faraday's law, the average reduction of reinforcement radius $\Delta r(t)$, the cross-sectional area $\Delta A_s(t)$, and average corrosion degree $\eta_{ave}(t)$ are respectively expressed by Eqs. (9), (10) and (11).

$$\Delta r(t) = \int_0^t 0.0116 i_{corr}(t) \, dt \tag{9}$$

$$\Delta A_s(t) = \pi d_0^2 - A_{ave}(t) = \pi d_0^2 - \pi \left[d_0 - 2 \cdot \Delta r(t) \right]^2 \tag{10}$$

$$\eta_{ave}(t) = \left[1 - A_{ave}(t)\right] / \left(\pi d_0^2\right) \tag{11}$$

where d_0 is the initial steel bar diameter; and $A_{ave}(t)$ is the average residual cross-sectional area of the corroded steel bar.

For the sake of simplicity, this paper evaluates the corrosion-induced crack width ω (mm) through an empirical model [45] based on the average reduction of cross-sectional area:

$$\omega(t) = 0.0575 \cdot \left[\Delta A_s(t) - \Delta A_{s0}\right],$$
$$\Delta A_{s0} = \pi d_0^2 \left\{1 - \left[1 - \alpha / d_0 \left(7.53 + 9.32 c_t / d_0\right) 10^{-3}\right]^2\right\} \quad (12)$$

where ΔA_{s0} represents the average reduction of the cross-sectional area once concrete cracks, c_t (mm) is the concrete cover of RC structures, and α is the pit concentration factor (α=2 for homogeneous corrosion but 4<α<8 for localized corrosion) [45,46]. Uncertainty in crack widths associated with corrosion degree can be taken into account by considering the probability distribution of the factor α in Eq.(12).

Furthermore, considering the influence of corrosion-induced cracks on the durability performance of RC structures, the diffusion coefficients of chloride D_c^{ω} and humidity D_h^{ω} for cracked concrete are evaluated by Eqs.(13) [47] and (14) [48], respectively.

$$D_c^{\omega} = f_{\omega 1}(\omega) \cdot D_c^{*}(t),\ f_{\omega 1}(\omega) = 31.61\omega^2 + 4.73\omega + 1, \omega \geq 0.1mm \quad (13)$$

$$D_h^{\omega} = f_{\omega 2}(\omega) \cdot D_h^{*}(t),\ f_h(\omega) = 1 + k_h \cdot \omega^3 / s_h \quad (14)$$

where k_h is an environmental parameter (10^5 mm^{-2} [48]); and s_h is the mean crack which is assumed to be 250 mm in this study [48].

3.2.Mechanical capacity of a corroded RC beam

This study investigated the mechanical behavior of a simply supported corroded RC beam with a rectangular cross-section (Fig. 2). The total and effective length, concrete cover, and stirrup spacing of the beam are l, l_{eft}, c, and s_v, respectively, and the cross-sectional width, total height, and effective height are denoted as b, h, and h_0, respectively. Existing studies proved that chloride attack generally induced non-uniform reinforcement corrosion, which further causes spatial variability in the mechanical capacities of corroded RC beams. Therefore, failure could occur in other positions than span mid-point [49,50]. To account for the spatial variability, the beams are separated into m zones concerning the spatial effects of corrosion non-uniformity on the mechanical performance of RC beams, as shown in Fig. 2.

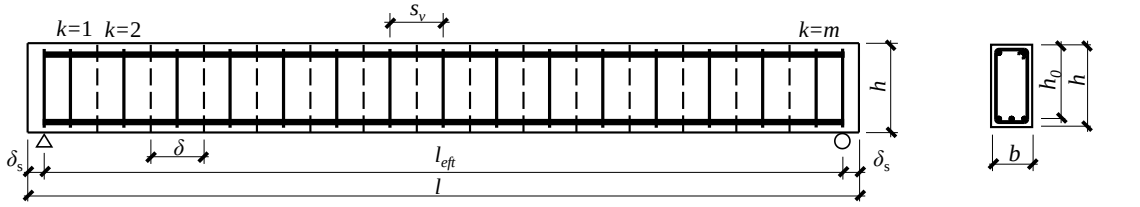

(a) Layout of RC beam (b) Cross-section of RC beam

Fig. 2 Geometry schematic of a simply-supported RC beam

Moreover, within each zone, the non-uniform reinforcement corrosion is quantified using the corrosion non-uniformity factor [49], denoted as $R_{k,j}$, to consider the corrosion non-uniformity of the j-th steel bar in the k-th zone.

$$R_{k,j}(t) = A_{ave}(t) / A_{\min,k,j}(t) \quad (15)$$

where $A_{\min,k,j}(t)$ represents the minimum cross-sectional area of the j-th tension bar in the k-th zone at time t. Similar approaches have been observed in previous studies [9,10,12].

Furthermore, by employing Eq.(15), the maximum corrosion degree $\eta_{max}(t)$ of steel bars varies with longitudinal and transverse directions.

Existing study shows that factor $R(t)$ follows a Gumbel distribution whose distribution parameters μ and σ could be computed by Eqs. (16) and (17), respectively [1,49]. For the sake of simplicity, the factor R and the minimum cross-sectional area of each zone are supposed to be independent of the others [13,49].

$$\mu(t) = 3.35 \cdot \eta_{ave}(t) \exp\left[-0.236 i_{corr}(t)\right] + 0.12 \cdot \eta_{ave}(t) + 1.01 \tag{16}$$

$$\sigma(t) = 0.3371 \eta_{ave}(t) + 0.0006 \tag{17}$$

Based on the autocorrelation analysis results from previous studies [49,51], it has been observed that the correlation coefficient decreases significantly for analysis lengths greater than 50 mm. Thus, the RC beam can be divided into multiple zones of not less than 50 mm in length, and treat the factor R of each zone and each bar as independent random variables [2,13,38]. This approach allows for the consideration of spatial correlation in the corrosion distribution.

3.2.1. Analytical mechanical models of RC beam

For the analytical models, the time-dependent bending and shear capacities of RC beams are computed separately based on several assumptions. For instance, supposing RC beams with planar sections are well-anchored and completely bonded during their service lives, their flexural capacities $M_{u,k}(t)$ at each zone can be calculated by Eq.(18) [13,49].

$$M_{u,k}(t) = F_{y,k}(t) \cdot \left[h_0 - 0.5 F_{y,k}(t) \big/ (b \cdot f_c)\right] \tag{18}$$

where f_c is the concrete compressive strength (MPa); and $F_{y,k}(t)$ (N) is the capacity of corroded tension rebars of the k-th zone at time t, which could be expressed by Eq.(19).

$$F_{y,k}(t) = f_{y0} \cdot A_k^t(t) \tag{19}$$

where f_{y0} is the yield strength of uncorroded tension bars; $A^t_k(t)$ is the equivalent cross-sectional area of tension bars in the k-th zone.

Considering the effects of corrosion on the ductility of corroded steel bars, $A^t_k(t)$ is computed by Eq.(20).

$$\begin{aligned} A_k^t(t) = & \max_{j=1}^{n_t}\left[j \cdot A^t_{\min,k,n_t+1-j}(t)\right] \cdot \left[1 - \prod_{j=1}^{n_t} H\left([R]_{cr} - R_{k,j}(t)\right)\right] \\ & + \sum_{j=1}^{n_t} A^t_{\min,k,j}(t) \cdot \prod_{j=1}^{n_t} H\left([R]_{cr} - R_{k,j}(t)\right) \end{aligned} \tag{20}$$

where n_t is the number of tension bars; $[R]_{cr}$ is the critical value of corrosion non-uniformity factor 1.3 [49]; $A^t_{\min,k,j}(t)$ is the minimum cross-sectional area (mm^2) of the j-th tension bar in ascending order in the k-th zone ($A^t_{\min,k,1}(t) < A^t_{\min,k,2}(t) <\cdots< A^t_{\min,k,n_t}(t)$); and $H(x)$ is the Heaviside function that equals 1 when the value inside parentheses ≥ 0 and 0 otherwise.

In addition, according to the classical truss models with a crack inclination angle of 45°, the shear bearing capacity $V_k(t)$ of any zone in the beam is given by Eq.(21) [11,12].

$$V_k(t) = V_c + V_{s,k}(t) = 1.75/(\lambda_s + 1) \cdot f_t b h_0 + F_{A_{v,k}}(t) \cdot h_0 / s_v \tag{21}$$

where V_c and $V_{s,k}$ are denoted as the contributions of concrete and stirrup components on shear capacity, respectively; f_t is the concrete tensile strength; λ_s is the shear-to-span ratio; $F_{Av,k}(t)$ is the vertical tensile capacity of stirrup bars under the k-th zone at time t.

Since only the vertical parts of the stirrup bars are considered for computing the shear capacity of RC beams, $F_{Av,k}(t)$ can be calculated by summing the tensile capacities of the vertical parts of all stirrups legs, as shown in Eq.(22).

$$F_{A_{v,k}}(t) = f_{yv0} A_k^s(t) = f_{yv0} \sum_{w=1}^{n_{sv}} A_{min,k,w}^s(t) \tag{22}$$

in which f_{yv0} is the yield strength of uncorroded stirrup bars; n_{sv} is the number of stirrup legs; $A_k^t(t)$ is the equivalent cross-sectional area sum of stirrup bars in the k-th zone; and $A_{min,k,w}^s(t)$ (k=1, 2, ..., m; w= 1,2, ..., n_{sv}) is the minimum cross-sectional area (mm^2) of the w-th stirrup bar of the k-th zone.

Eqs.(18)-(22) are directly applied to calculate $M_{u,k}$, and $V_{u,k}$ for each zone by the mechanical properties of the reinforcement and concrete and the cross-sectional areas of steel bars.

3.2.2. Finite element model of RC structures

Although the models presented in Section 3.2.1 offer an estimation of the mechanical capacity of RC beams over time, it is essential to acknowledge that such predictions might be prone to inaccuracies and require adjustments in the performance assessment. This is primarily because the models may not adequately account for the complex interaction between the mechanical properties of steel and concrete. Additionally, it is worth noting that the analytical models described in Section 3.2.1 do not consider the combined effects of bending and shear, which can result in limitations in accurately predicting the failure mode of RC beams.

To address the above issues, a FEM for corroded RC beams is employed to address such a concern, which could comprehensively consider realistic geometry and mechanical properties [17]. The total strain-based crack model is used for the concrete constitutive model [52]. As illustrated in Fig. 3a, the tensile concrete stress increases linearly before reaching the ultimate tensile strength and then drops following a tension-softening model developed by Hordijk [53]. The compressive concrete stress increases/decreases following parabolic curves [54]. In addition, as shown in Fig. 3b, a corrosion degree-based trilinear constitutive model of corroded steel bars is adopted [55], where the elastic modulus E_{s0}, actual yield strength f_{y0}, and ultimate strength of corroded steel bar f_{u0} remain unchanged [56,57]. Besides, hardened strain ε_{sh} and ultimate strain ε_{su} decrease with the maximum corrosion degree η_{max}, which could be expressed by Eqs. (23) and (24) [58–60].

$$\varepsilon_{sh} = \begin{cases} f_{y0}/E_{s0} + (\varepsilon_{sh0} - f_{y0}/E_{s0})(1 - \eta_s/\eta_{s,cr}), \eta_{max} \le \eta_{cr} \\ \varepsilon_{sy} = f_{y0}/E_{s0}, \eta_{max} > \eta_{cr} \end{cases} \tag{23}$$

$$\varepsilon_{su} = \exp(-2.501\eta_{max})\varepsilon_{su0} \tag{24}$$

where η_{cr} is the critical corrosion degree [12,61]; and ε_{sh0} and ε_{su0} are the hardened strain and ultimate strain of non-corroded steel bars.

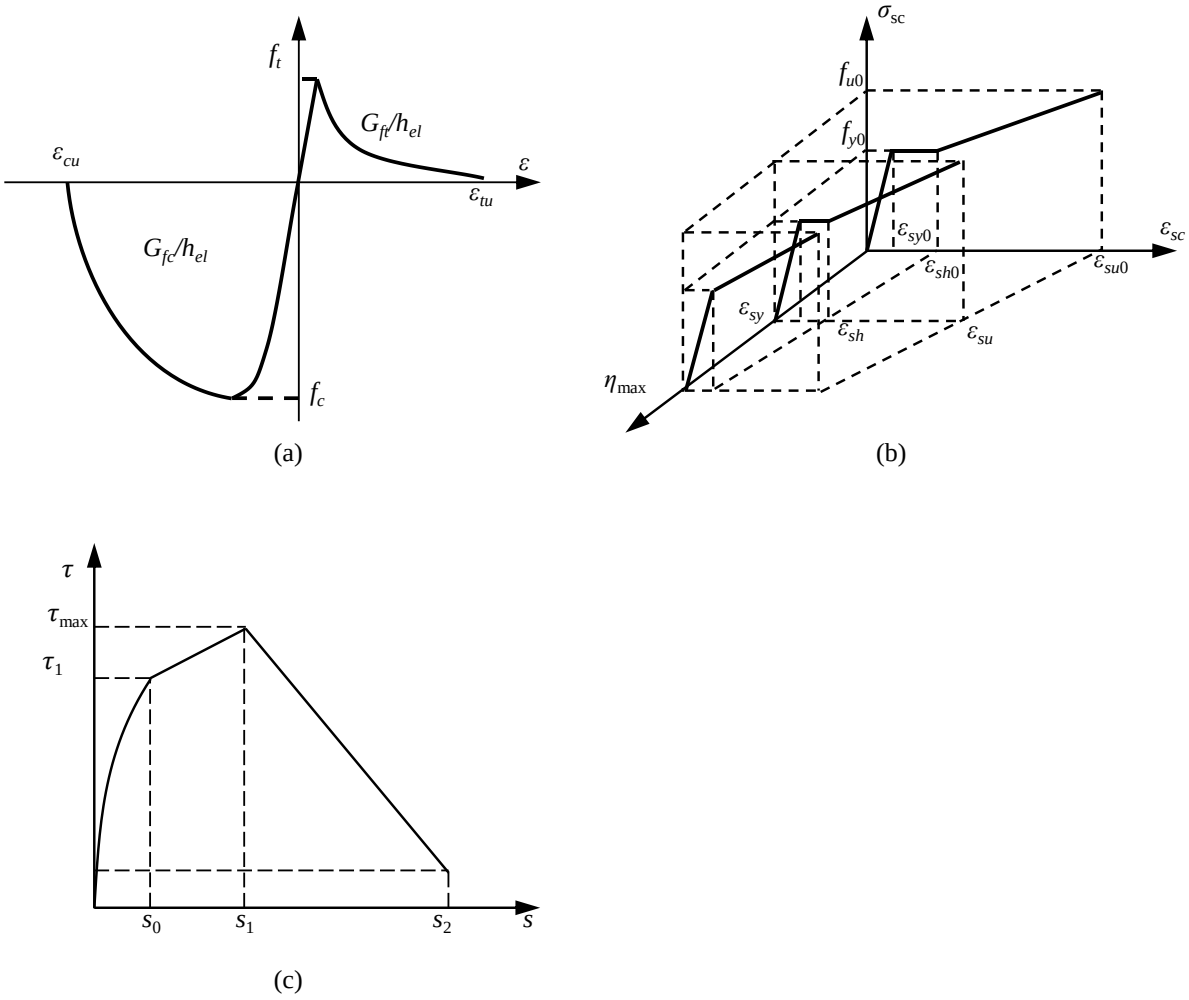

Fig. 3 Schematics of constitutive models for different materials: (a) concrete; (b) reinforcement; and (c) bond-slip

Moreover, different from the analytical models in Section 3.2.1, the bond-slip constitutive model is considered in FEM by directly assigning it to the interface between steel bar and concrete, as shown in Fig. 3c. The bond stress τ of corroded steel bars versus slip s could be written as [62]

$$\tau = \begin{cases} \tau_1 \left(s / l_1 \right)^{0.3}, 0 \le s < s_0 \\ \left(s - s_0 \right) \Big/ \left(s_1 - s_0 \right) \cdot \left(1 - 0.7 \right) \cdot \tau_{max} + 0.7 \cdot \tau_{max}, s_0 \le s < s_1, \\ \left(s - s_1 \right) \Big/ \left(s_1 - s_2 \right) \cdot \left(1 - 0.3 \right) \cdot \tau_{max} + \tau_{max}, s_1 \le s < s_2 \end{cases}$$

$$\tau_1 = 2.57 f_c^{0.5}, s_0 = 0.15 c_0 \left(\alpha_{bond} \tau_{max} \Big/ \tau_1 \right)^{1/0.3}, \quad (25)$$

$$s_1 = 0.15 c_0 \exp\left[(1/0.3) \ln(\tau_{max} / \tau_1) \right] + 0.4 \ln\left(\tau_1 / \tau_{max} \right)$$

where c_0 is the rib spacing; s_2 is $0.35c_0$, respectively; and τ_{max} is the maximum bond strength of RC beams, which could be evaluated by an empirical model [63]:

$$\tau_{max} = (k_1 + k_2\eta_{ave})\left[0.55 + 0.24(c/d_t)\right]\sqrt{f_c} + 0.191 \cdot A_{sv} f_y / (s_v \cdot d_t) \quad (26)$$

where c is the concrete cover; d_t is the diameter of the tension bar; A_{sv} is the cross-sectional area of stirrup bars; and k_1 and k_2 are the factors of the reduced contribution of concrete towards bond strength [64].

Given the geometric model, boundary conditions, constitutive model, and loading pattern, the FEM can be used to capture the comprehensive information (i.e., strains and stress of reinforcement and concrete, mid-span deflection, and reaction loads at supports) at each load step. Besides, in this study, three limit states are considered including ultimate limit state (ULS) and two serviceability limit states (SLS): SLS1 (0.05 mm loading concrete crack [65]) and SLS2 (1 mm severe loading concrete crack [66]). The critical external loads at the SLS, denoted as $P_{FEM,si}$ (i=1,2), and ULS, denoted as $P_{FEM,u}$ could be calculated according to the reaction loads and corresponding mechanical information [17].

The failure mode F_{mod} of RC beams can be determined according to the sequence of the individual events: stirrup bars breaking, tension bars breaking, and concrete crushing, where the first one is regarded as a shear failure F_{mod}=0 and the latter two are considered to be flexural failures F_{mod}=1[17].

3.3.Time-dependent reliability analysis

For time-dependent reliability analysis, the initial step involves establishing the performance functions $g(\boldsymbol{\theta}, t)$ for different limit states and their corresponding critical loads, such as P_u, P_{s1}, and P_{s2}. Taking the ULS as an example, the performance function for P_u could be formulated as follows:

$$g_u(\boldsymbol{\theta}, t) = P_u(\boldsymbol{\theta}, t) - S(\boldsymbol{\theta}, t) \quad (27)$$

in which $\boldsymbol{\theta}$ is the vector containing all input variables; and P_u ($\boldsymbol{\theta}$, t) and S ($\boldsymbol{\theta}$, t) are the ultimate capacities and external load at a given time instant t and $\boldsymbol{\theta}$, respectively.

Accordingly, considering the first passage issue, the time-dependent failure probability $p_{f,u}(t)$ could be described as the probability that $g_u(\boldsymbol{\theta}, t)$ reaches the critical value within a given time interval [0,t], i.e., Eq.(28).

$$p_{f,u}(t) = \Pr\left\{g_u(\boldsymbol{\theta}, \tau) \le 0, \tau \in [0, t]\right\} \quad (28)$$

Similarly, regarding the two SLSs, their performance function $g_{si}(\boldsymbol{\theta}, t)$ (i=1 and 2) and corresponding time-dependent probability $p_{f,si}(t)$ could be expressed by Eqs. (29) and (30).

$$g_{si}(\boldsymbol{\theta}, t) = P_{si}(\boldsymbol{\theta}, t) - S(\boldsymbol{\theta}, t), (i = 1, 2) \quad (29)$$

$$p_{s,i}(t) = \Pr\left\{g_{si}(\boldsymbol{\theta}, \tau) \le 0, \tau \in [0, t]\right\}, (i = 1, 2) \quad (30)$$

The essential step of solving $p_{f,u}(t)$ and $p_{s,i}(t)$ is to accurately capture the probabilistic distribution information for the critical extern loads via the models in Section 3.2. Although FEM is potent in accurately calculating the mechanical information of RC structures, it is not as straightforward as analytical models in estimating the capacities of RC structures over time. Therefore, inspired by previous studies [29,67], a suboptimal strategy is applied to apply

adjustment coefficients (α_{s1}, α_{s2}, and α_u) to modify the results of the analytical models based on the FEM results.

$$\alpha_{si}(\boldsymbol{\theta},t) = P_{\mathrm{FEM},si}(\boldsymbol{\theta},t) \big/ P_{\mathrm{ana}}(\boldsymbol{\theta},t), \alpha_{\mathrm{u}}(\boldsymbol{\theta},t) = P_{\mathrm{FEM,u}}(\boldsymbol{\theta},t) \big/ P_{\mathrm{ana}}(\boldsymbol{\theta},t), (i=1,2) \tag{31}$$

where $P_{FEM,si}$ is the critical load computed from FEM given the limit state, input variables, and time t; and P_{ana} is the ultimate load computed based on the analytical models as

$$P_{\mathrm{ana}}(\boldsymbol{\theta},t) = \min\left\{P_{M_u}(\boldsymbol{\theta},t), P_{V_u}(\boldsymbol{\theta},t)\right\} \tag{32}$$

where P_{Mu} and P_{Vu} are the loading capacities of flexural and shear capacities based on the $M_{\mathrm{u},k}$, and $V_{\mathrm{u},k}$ (k=1,2…m) and the loading pattern of RC beams. According to Eqs. (31) and (32), given the adjustment coefficients, the adjusted loading capacities subject to different limit states could be expressed by Eq. (33).

$$P_u(\boldsymbol{\theta},t) = \alpha_u(\boldsymbol{\theta},t) \cdot P_{ana}(\boldsymbol{\theta},t), P_{si}(\boldsymbol{\theta},t) = \alpha_{si}(\boldsymbol{\theta},t) \cdot P_{ana}(\boldsymbol{\theta},t) \tag{33}$$

4. Bayesian network developments

4.1.Static and Dynamic Bayesian networks

A BN is applied to represent a joint probability distribution concerning a set of random variables (called nodes in BN) $X_{1:n_{bn}}=\{X_1, X_2,\ldots, X_{n_{bn}}\}$ (n_{bn} is the number of nodes) and consists of two parts: a directed acyclic graph (DAG) with vertices and edges corresponding to nodes X_{bn} and their dependencies; and the probability distribution information of all nodes.

Generally, two types of BN exist, i.e., static BN (SBN) and dynamic BN (DBN). The former contains only a one-time slice for time-independent variables, and the latter is adopted to depict the time dependencies among variables, e.g., c_{bar}, i_{corr}, and P_{u}. DBN contains a series of time-slice BNs with a set of random variables $X^{i}_{1:n_{bn}}=\{X_1^i, X_2^i,\ldots, X^i_{n_{bn}}\}$ (i=1,2,..., T) at different time steps [28]. Within DBNs, the joint probability distribution $P(X^{1}_{1:n_{bn}},\ldots, X^{T}_{1:n_{bn}})$ of all nodes over time T is denoted as $P\left(X^{1:T}_{1:n_{bn}}\right)$, expressed by Eq.(34) via adopting the Markov assumption [30]:

$$P\left(X^{1:T}_{1:n_{bn}}\right) = \prod_{i=1}^{T-1} P\left(X^{i+1}_{1:n_{bn}} \mid X^{i}_{1:n_{bn}}\right) \tag{34}$$

where $P\left(X^{i+1}_{1:n_{bn}} \mid X^{i}_{1:n_{bn}}\right)$ denotes the conditional probability distribution at the i+1-th time slice given the probability information of nodes at the i-th time slice. Due to Markov's assumption and Eq. (34), T time slices of DBN can be built by unrolling the first two time slices of DBN, effectively reducing the difficulty of DBN modeling.

For exact inference, only discrete random variables are concerned. To perform exact inference for continuous random variables, discretization is implemented. Besides, the conditional probability mass functions (PMF) of all nodes are expressed by the conditional

probability table (CPT). The procedure of node discretization and CPT computation are outlined in Appendix A1 [2]. Then, supposing a n_{bn} nodes of SBN and given an evidence combination $y_{1:n2}=(y_1, y_2,\ldots, y_{n2})$ of inspection nodes $Y_1,Y_2,\ldots,Y_{n2}$ (n_2 is the number of inspection nodes), the joint PMF of residual n_1 (i.e., $n_{bn} - n_2$) nodes $X_1, X_2,\ldots,X_{n1}$ could be expressed by

$$P\left(X_1 = x_1,\ldots, X_{n_1} = x_{n_1} \mid Y_1 = y_1,\ldots, Y_{n_2} = y_{n_2}\right) = \frac{\prod_i P\left(y_i \mid \mathrm{Pa}\left(y_i\right)\right)\prod_j P\left(x_j \mid \mathrm{Pa}\left(x_j\right)\right)}{\sum_{x_1,\ldots,x_{n_1}}\prod_i P\left(y_i \mid \mathrm{Pa}\left(y_i\right)\right)\prod_j P\left(x_j \mid \mathrm{Pa}\left(x_j\right)\right)}, i = 1,\ldots, n_2,\ j = 1,\ldots, n_1 \tag{35}$$

where $\mathrm{Pa}(y_i)$ is the set of parent nodes of Y_i.

For T time slices of DBN, supposing a set of evidence combinations at all time slices $\{y_{1:m}^1,\ldots, y_{1:m}^T\}=\{y_1^1,\ldots, y_{n2}^1,\ldots, y_1^T,\ldots, y_{n2}^T\}$, the joint PMF of residual n_1 (i.e., $n_{bn} - n_2$) nodes could be written as

$$P\left(X_{1:n_1}^1 = x_{1:n_1}^1,\ldots, X_{1:n_1}^T = x_{1:n_1}^T \mid Y_{1:n_2}^1 = y_{1:n_2}^1,\ldots, Y_{1:n_2}^T = y_{1:n_2}^T\right) = \frac{\prod_{u,v} P\left(y_v^u \mid \mathrm{Pa}\left(y_v^u\right)\right)\prod_{p,q} P\left(x_q^p \mid \mathrm{Pa}\left(x_q^p\right)\right)}{\sum_{x_{1:n_1}^1,\ldots,x_{1:n_1}^T}\prod_{u,v} P\left(y_v^u \mid \mathrm{Pa}\left(y_v^u\right)\right)\prod_{p,q} P\left(x_q^p \mid \mathrm{Pa}\left(x_q^p\right)\right)},$$
$$u = 1,\ldots, T,\ v = 1,\ldots, n_2,\ p = 1,\ldots, T,\ q = 1,\ldots, n_1 \tag{36}$$

where $\mathrm{Pa}(y_q^p)$ is the set of parent nodes of Y_q^p.

Evidence that is a series of definite values is called hard evidence. Correspondingly, if the evidence obtained for the inspection nodes is a series of distributions, it is called uncertain evidence or soft evidence [68,69]. Denoting the inspection status of node Y_i and Y_v^u in SBN and DBN as y_{io} and y_{vo}^u, respectively, $P(Y_i= y_{is})$ and $P(Y_v^u= y_{vs}^u)$ are the probabilities of the s-th status of Y_i and Y_v^u. Then, Eqs.(35) and (36) could be rewritten to Eqs. (37) and (38), respectively.

$$P\left(X_1 = x_1,\ldots, X_{n_1} = x_{n_1} \mid Y_1 = y_{1o},\ldots, Y_{n_2} = y_{n_2 o}\right) = \frac{\sum_{y_{1:n_2 s}}\prod_j P\left(x_j \mid \mathrm{Pa}\left(x_j\right)\right)\prod_i \left[P\left(y_i \mid \mathrm{Pa}\left(y_i\right)\right) P\left(Y_i = y_{is}\right)\right]}{\sum_{x_1,\ldots,x_{n_1}, y_{1:n_2 s}}\prod_j P\left(x_j \mid \mathrm{Pa}\left(x_j\right)\right)\prod_i \left[P\left(y_i \mid \mathrm{Pa}\left(y_i\right)\right) P\left(Y_i = y_{is}\right)\right]},$$
$$i = 1,\ldots, n_2,\ j = 1,\ldots, n_1, s = 1, 2,\ldots. \tag{37}$$

$$P\left(X_{1:n_1}^1 = x_{1:n_1}^1,\ldots, X_{1:n_1}^T = x_{1:n_1}^T \mid Y_{1:n_2}^1 = y_{1:n_2 o}^1,\ldots, Y_{1:n_2}^T = y_{1:n_2 o}^T\right) = \frac{\sum_{y_{1:n_s s},\ldots,y_{1:n_s s}^T}\prod_{p,q} P\left(x_q^p \mid \mathrm{Pa}\left(x_q^p\right)\right)\prod_{u,v}\left[P\left(y_{vs}^u \mid \mathrm{Pa}\left(y_{vs}^u\right)\right)\cdot P\left(Y_v^u = y_{ys}^u\right)\right]}{\sum_{x_{1:n_1}^1,\ldots,x_{1:n_1}^T, y_{1:n_s s}^1,\ldots,y_{1:n_s s}^T}\prod_{p,q} P\left(x_q^p \mid \mathrm{Pa}\left(x_q^p\right)\right)\prod_{u,v}\left[P\left(y_{vs}^u \mid \mathrm{Pa}\left(y_{vs}^u\right)\right)\cdot P\left(Y_v^u = y_{ys}^u\right)\right]},$$
$$u = 1,\ldots, T,\ v = 1,\ldots, n_2,\ p = 1,\ldots, T,\ q = 1,\ldots, n_1, s = 1, 2,\ldots \tag{38}$$

The above BN inference is achieved by a frontier algorithm, including a smoothing strategy for both forward and backward operators to reduce the time complexity of DBN inference [28].

4.2.Mixed Bayesian network for reliability analysis of RC structures

The integration of all physical models and random variables from Section 3 into a giant DBN and implementing BN inference pose formidable challenges, primarily due to the increasing number of time slices, nodes, and links [19,20]. Existing studies often resort to crude simplifications by directly reducing nodes or links within BNs [30,34]. However, such simplifications may result in the loss of valuable probabilistic information, lacking the necessary physical mechanisms and theoretical support for reliable probabilistic inference and reliability analysis.

To address the limitations of existing DBN analysis methods, this study introduces a novel approach called Mixed Bayesian Network (MBN). The fundamental idea behind MBN is to build sub-BNs, including both static BNs and dynamic BNs, based on various physical and mathematical models. These sub-BNs are then connected using pinch-point variables to facilitate reliability analysis under different limit states, as shown in Fig. 4. This innovative MBN approach not only enables objective modeling and inference of the original DBN but also dramatically simplifies the complexity of the process and improves analysis efficiency. Thus, MBN enables a comprehensive reliability analysis of RC beams, involving multiple sub-BNs (DBNs and SBNs) for integrated analysis.

In the MBN, each node represents a sub-BN and its output variables, such as i_{corr}, Δr, and P_{Mu}. The 'blue nodes' represent DBNs for durability assessment (e.g., 'i_{corr}' and 'Δr'), while the 'white nodes' represent SBNs for adjustment factors and failure modes of FEM (e.g., 'α_x' and 'F_{mod}'). These output variables serve as shared nodes between adjacent sub-BNs, acting as pinch-point variables to connect them. For instance, the inspection results of corrosion-induced crack width ω in the DBNs of 'i_{corr}' and 'Δr' can update the Probability Mass Functions (PMFs) of the pinch-point variables i_{corr} and Δr. These updated PMFs then work as soft evidence for the nodes of i_{corr} and Δr in the DBNs of 'P_{Mu}' and 'P_{Vu}', as well as in the SBNs of 'α_x' and 'F_{mod}'. Similarly, the updated PMFs of the P_{Mu} and P_{VU} nodes in 'P_{Mu}' and 'P_{Vu}' can serve as soft evidence for the DBN updating of 'g_x'.

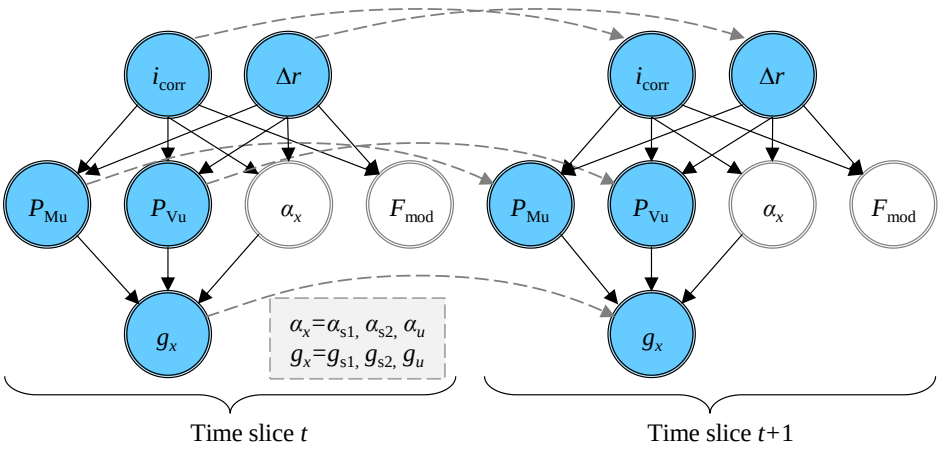

Fig. 4 MBN for reliability assessment of RC beams

The node discretization, CPT computation, and inference process of MBN are consistent with SBN and DBN in Section 4.1. The primary merit of MBN is that there is no need to oversimplify any sub-BNs in the model deliberately, and the critical physical information of each BN is retained as much as possible, making MBN potentially more accurate relative to a simplified BN. In addition, due to the modular feature of MBN, the structure of each sub-BN and the probabilistic information of the nodes can be conveniently replaced according to the requirements.

According to MBN in Fig. 4 and models in Section 3, other sub-BNs are introduced in the following. An SBN based on FEM is built to introduce the information for the variables α_x and F_{mod}, as illustrated in Fig. 5. Other critical input variables, such as i_{corr}, Δr, A_k^t (k=1, 2,…,m), and A_k^s (k=1, 2,…,m), are also extracted as nodes for this SBN. Moreover, the parent-child relationship of these nodes is determined, e.g., A_k^t is a child node of i_{corr} and Δr but a parent node of α_x, as shown in Fig. 5. Given the updating information of i_{corr} and Δr at any time instant, this SBN could provide the updating information of α_x and F_{mod} accordingly. Furthermore, the available studies prove that not every cross-section contributes to the mechanical properties of the corroded RC beams [17]. Therefore, for the sake of simplicity, the number of A_k^t and A_k^s investigated in Fig. 5 can be limited based on the sensitivity analysis results.

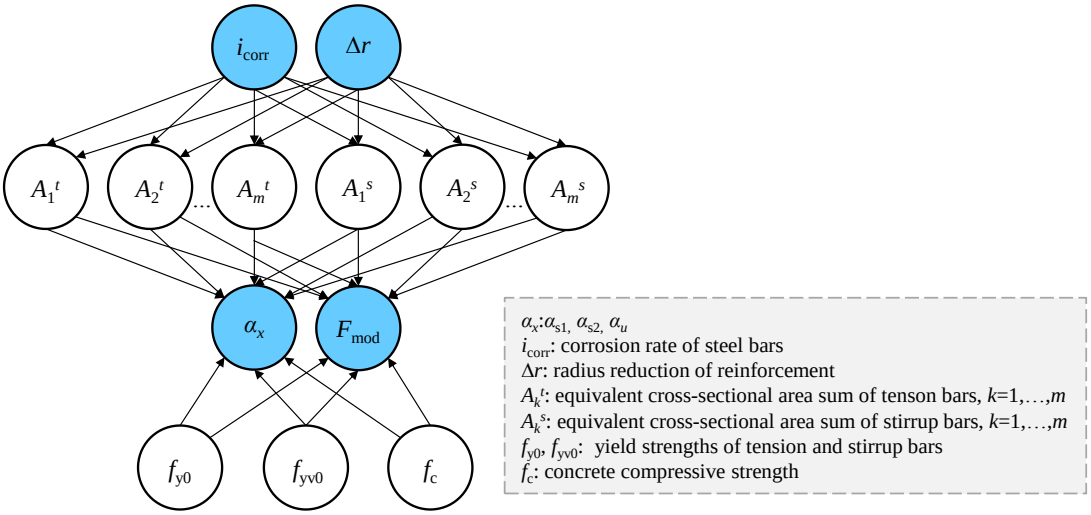

Fig. 5 SBN of FEM for corroded RC beams

Besides, other sub-BNs, including durability assessment, analytical capacity calculation, and reliability assessment, are established via DBNs, as presented in Fig. 6a, b, and c, where arc-shaped dashed arrows indicate the time dependence between adjacent time slices. Also, similar to Fig. 5, the numbers of A_k^t and A_k^s investigated could be appropriately reduced by the sensitivity analysis results. Besides, for the DBN relating to time-dependent reliability analysis (Fig. 6c), the probabilistic information of some input variables needs to be captured by the SBN of FEM in each time slice.

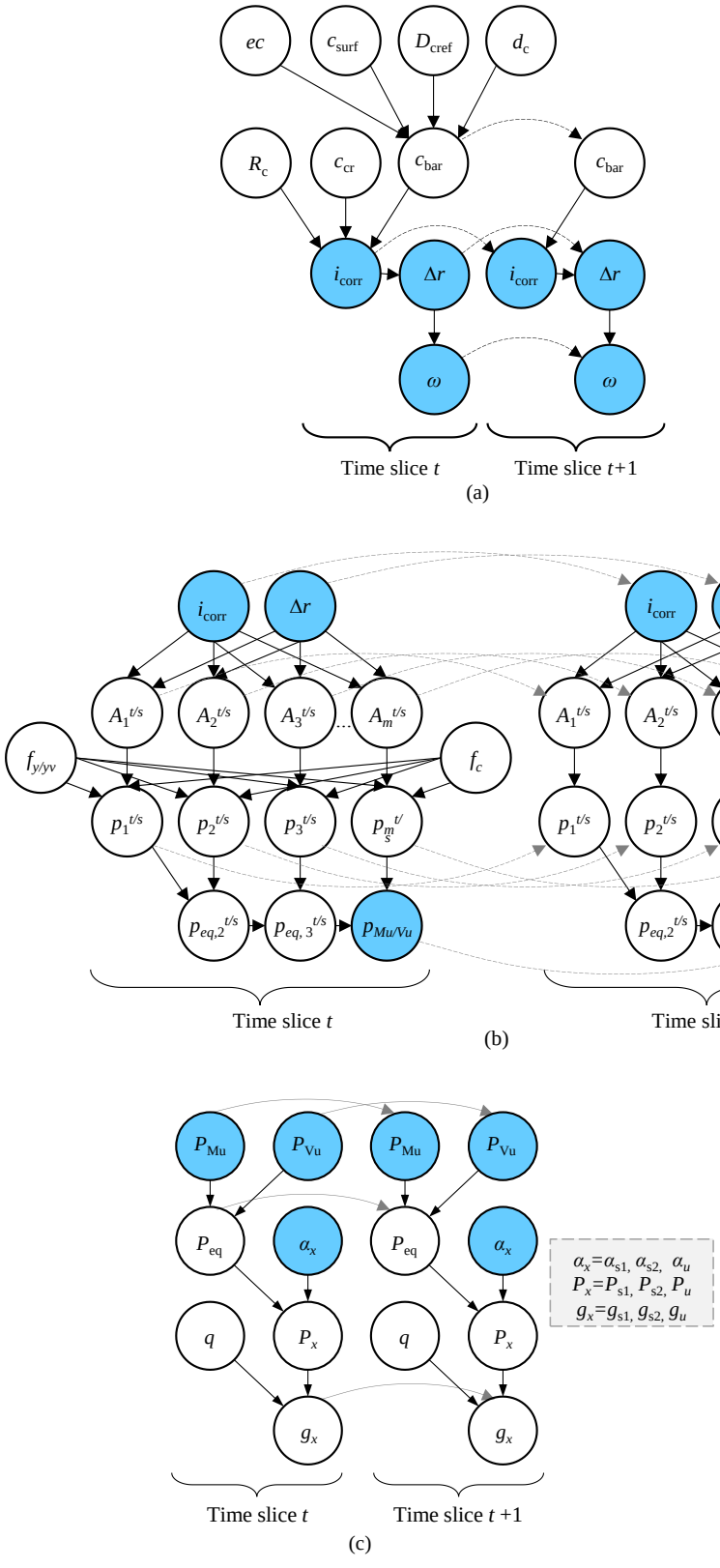

Fig. 6 DBNs for other models: (a) chloride-induced durability assessment; (b) analytical capacities of corroded RC beam; and (c) time-dependent reliability analysis

5. Illustrative examples

5.1.Description

To illustrate and study the efficiency of the developed framework, a simply supported RC beam with a cross-section of 150×300 mm is assumed to be located on the west coast of the Yellow Sea since 2010, as displayed in Fig. 2 [1]. The parameters of the geometry and reinforcement layout of the beam are listed in Table 1.

Table 1 Geometry parameters and reinforcement of the studied RC beams

Parameters	Value
Total length l	5400 mm
Effective section height h_0	275 mm
Section width b	150 mm
Initial diameter of tension bars d_{t0}	20 mm
Initial diameter of compression bars $d_{t'0}$	12 mm
Initial diameter of stirrup bars d_{sv0}	6 mm
Effective length l_{eft}	5000 mm
Stirrup spacing s_v	250 mm
Number of tension bars n_t	3
Number of compression bars $n_{t'}$	2
Number of stirrup bars n_{sv}	2
Number of zones m	20

Regarding the environmental and durability assessment, the parameters for environmental models $f(ec, t)$ were obtained from previous studies [1,70]. Fig. 7 presents an example of the variation of environmental parameters, including temperature T, relative humidity RH, and chloride deposition C_{surf}, assuming ec = 2°C. As shown, this example accounts for the periodicity, time dependence, and nonlinearity within the variations of environmental parameters. In addition, the distribution types and parameters of isolated parent nodes in all sub-BNs (Fig. 5 and Fig. 6) are listed in Table 2.

The following sections focus on building MBN and presenting the time-dependent reliability analysis by integrating the inspection results. The former is described in Section 5.2, and the latter will be presented in Sections 5.3 and 5.4.

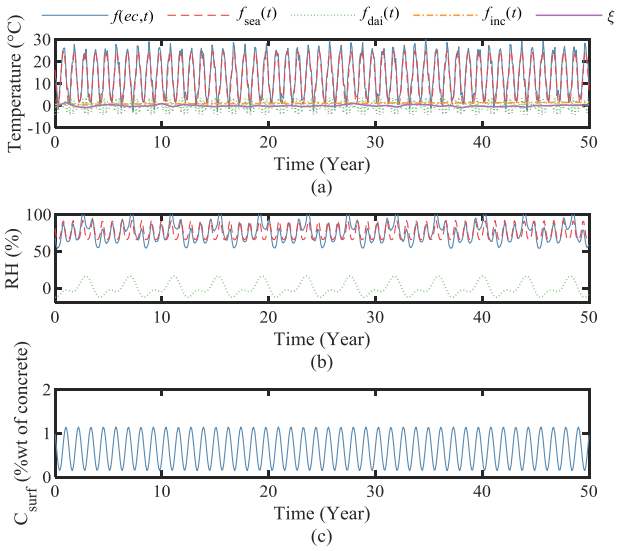

Fig. 7 Schematics of environmental model: (a) temperature; (b) humidity; and (c) chloride deposition

Table 2 Distribution types and values of parent nodes in sub-BNs

Parameters	Distribution	μ	δ	Ref
Characteristic exposure conditions *ec*(°C)	Uniform	0	3.5	[1]
A baseline of chloride deposition c_{surf0} (wt% of cement)	Gaussian*	0.65	0.1	[1]
Reference coefficient of chloride diffusion D_0(10^{-11} m^2/s)	Lognormal	1.6	0.1	[71]
Concrete cover c (mm)	Gaussian*	25	0.05	[72]
Critical chloride content c_{cr} (wt% of cement)	Lognormal	0.4	0.1	[14]
Resistance of concrete cover R_c(kΩ)	Lognormal	25	0.1	[39]
Compressive strength of concrete f_c (MPa)	Gaussian*	25	0.15	[14]
Elastic modulus of reinforcement (MPa)	Gaussian*	2×10^5	0.02	[73]
Yield strength of longitudinal bars (MPa)	Gaussian*	360	0.05	[74]
Yield strength of stirrup bars (MPa)	Gaussian*	220	0.05	[73]

Note: μ and δ are the lower and upper bounds for the uniform distribution value, while μ and δ are the mean and coefficient of variation (COV) for other distributions; * means that the variable is truncated at 0.

5.2.MBN establishment

Before building the MBN for the RC beam, some preparations must be completed to obtain a priori information on all nodes in MBNs, and their probabilistic information is captured from representative samples. To select representative samples, the good-lattice-point-set-partially stratified-sampling (GLP-PSS) based method was adopted to generate 610 representative samples (following the Fibonacci sequence) based on the distribution information of isolated parent nodes as shown in Table 2 [2,75]. Given the values of isolated parent nodes for each representative sample, the values of all other nodes could be computed based on the deterioration models mentioned in Sections 3.1-3.2.

To reduce the computational burden, the MBN is simplified by reducing the number of time slices, nodes, and links. For the purpose of demonstration and to align with previous research [2], a time interval of 3 years and 18 time slices are chosen. This decision is based on the knowledge that using smaller time intervals and an excessive number of slices do not

yield significant benefits. Moreover, each node is assigned 8 discrete statuses, except for certain binary nodes g_x (g_{s1}, g_{s2}, and g_u).

On the other hand, considering corrosion non-uniformity, RC beams are divided into m zones with a large number of random variables associated with the cross-sectional area of the corroded reinforcement (A_k^t and A_k^s, k=1, 2, ..., m) (Section 3.2), which also brings a burden on the MBN inferential analysis. Thus, sensitivity analysis is implemented to investigate the contributions of each spatial zone to the mechanical performance of RC beams. As illustrated in Fig. 8, the probability of ULS occurrence in each spatial zone is calculated based on the results of 610 representative samples over 50 years. Fig. 8a and b both indicate that flexural failure events are concentrated at the midspan of the RC beam, while shear failure events are concentrated near the supports of the RC beam, especially in the analytical models (Fig. 8a). Such a phenomenon is consistent with the previous reliability related studies [10,76].

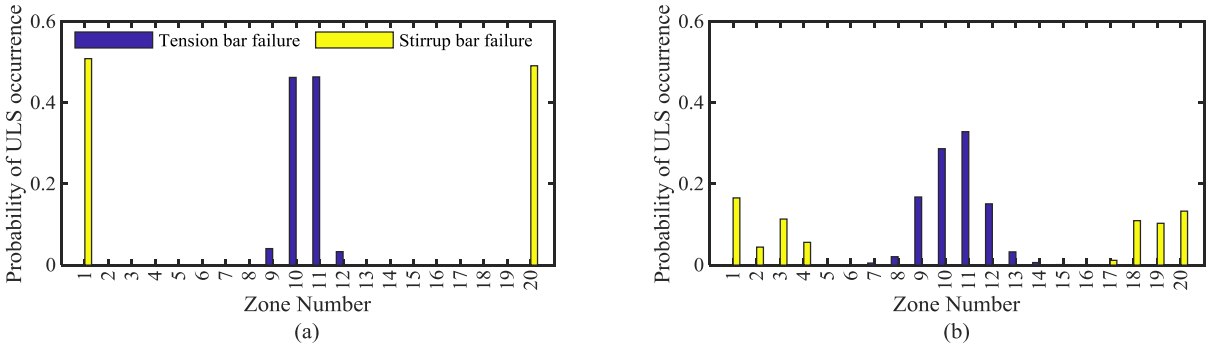

Fig. 8 Probability distribution of ULS occurrence caused by non-uniform corrosion over 50 years: (a) analytical mechanical model; and (b) FEM

In addition, Fig. 8 also demonstrates that the spatial distribution of the ULS occurrences of the analytical model differs from FEM results so that the sub-BNs are simplified in different ways. Among the sub-BNs associated with the analytical model (Fig. 6b), the 9th to 12th zones (i.e., A_9^t to A_{12}^t) are of interest for flexural failure, and the 1st and 20th zones (i.e., A_1^s and A_{20}^s) are of interest for shear failure. Regarding the sub-BNs of the FEM (Fig. 5), the 8th to 13th zones (i.e., A_8^t to A_{13}^t) are of interest for flexural failure; the 1st to 4th zones (i.e., A_1^s to A_4^s) and 17th to 20th zones (i.e., A_{17}^s to A_{20}^s) are of interest for shear failure. However, since analytical models lack consideration for the combined effects of bending and shear, Fig. 8a may potentially be misleading in terms of the failure modes. Therefore, in the formal discussion for the failure mode of RC beams, only FEM-based results will be utilized in MBN (Section 5.3.4).

According to Appendix A.1, all nodes in MBNs are discretized into discrete nodes, and their CPTs are computed accordingly. Besides, it is worth noting that the pinch-point variables in MBN own two CPTs since they simultaneously serve as parent and child nodes in adjacent sub-BNs.

5.3.Inference results

Once the MBN is established, the following task is to infer and evaluate the performance of RC beams. Supposing the probability of detection (PoD) equals one, the width ω of

corrosion-induced concrete crack could be detected at several inspection instants (i.e., 3, 12, 21, 30, and 39 years). Additionally, in this scenario, the crack widths inspected at the beam surface exhibit a certain statistical range, where potential inspection results of ω (mm) are assumed as follows: $\omega_1 \in [0, 0.1]$, $\omega_2 \in [0.2, 0.3]$, and $\omega_3 \in [0.5, 0.6]$ [2]. The MBN was applied to infer critical parameters of the structural performance of RC beams subjected to different inspections, such as the flexural and shear capacity P_{Mu} and P_{Vu}, adjustment coefficients α_x, and limit state variable g_x. Since durability assessments such as chloride content and corrosion rates c_{bar} and i_{corr} on the steel surface have been explored in detail in a previous study [2], these will not be discussed again in this study.

5.3.1. PMF of critical nodes in MBN

To demonstrate the effectiveness of the proposed framework, some classical scenarios are picked up to exhibit a priori and a posteriori PMFs of critical parameters, as illustrated in Fig. 9. As shown, the 3rd year inspection of ω_2 affects the PMFs of all parameters over time, while the 39th year inspection of ω_1 essentially has little effect on the PMFs before 39 years. Also, compared to no inspection, the earlier inspection results in higher PMFs in the negative axis direction for P_{Mu} and P_{Vu}, while the later inspection increases PMFs in the positive axis direction. For instance, in Fig. 9b and c, given the 3rd year inspection of ω_2, the probability of P_{Mu} in the range of 20.1 to 21.7 (kN) in 39 years increases by 241.7% compared to no inspection, while that in the range of 23.3 to 24.8 decreases by 99%; the probability of P_{Vu} in the range of 19.2 to 20.6 (kN) increases by 644.0% while that in the range of 23.3 to 24.6 (kN) decreases by 99.1%. This result matches common sense, as wider cracks indicate higher corrosion and lower load-bearing capacity and vice versa.

However, the scenario is slightly different for α_x. In 3 years, considering the 3rd year inspection of ω_2, the probability of α_1 in the range of 0.38 to 0.41 decreases by 32.5%, and that in the range of 0.41 to 0.43 increases by 26.1%. In 21 years, the inspection has little effect on the PMF of α_2. Besides, in 39 years, considering the 3rd year inspection of ω_2, the probability of α_{u} in the range of 0.88 to 0.94 increased by 43.7%, and that in the range of 0.94 to 0.99 decreased by 30.1% - the vice versa for the 39th year inspection of ω_1. Thus, the effects of inspection results on the adjustment coefficients of SLS might not be as significant as ULS. In addition, different from P_{Mu} and P_{Vu}, the adjustment ratio might not decrease with the corrosion degree for SLS.

In the following, the influence of different test results on the mechanical capacity and the probability and mode of failure at different limit states are discussed in further detail.

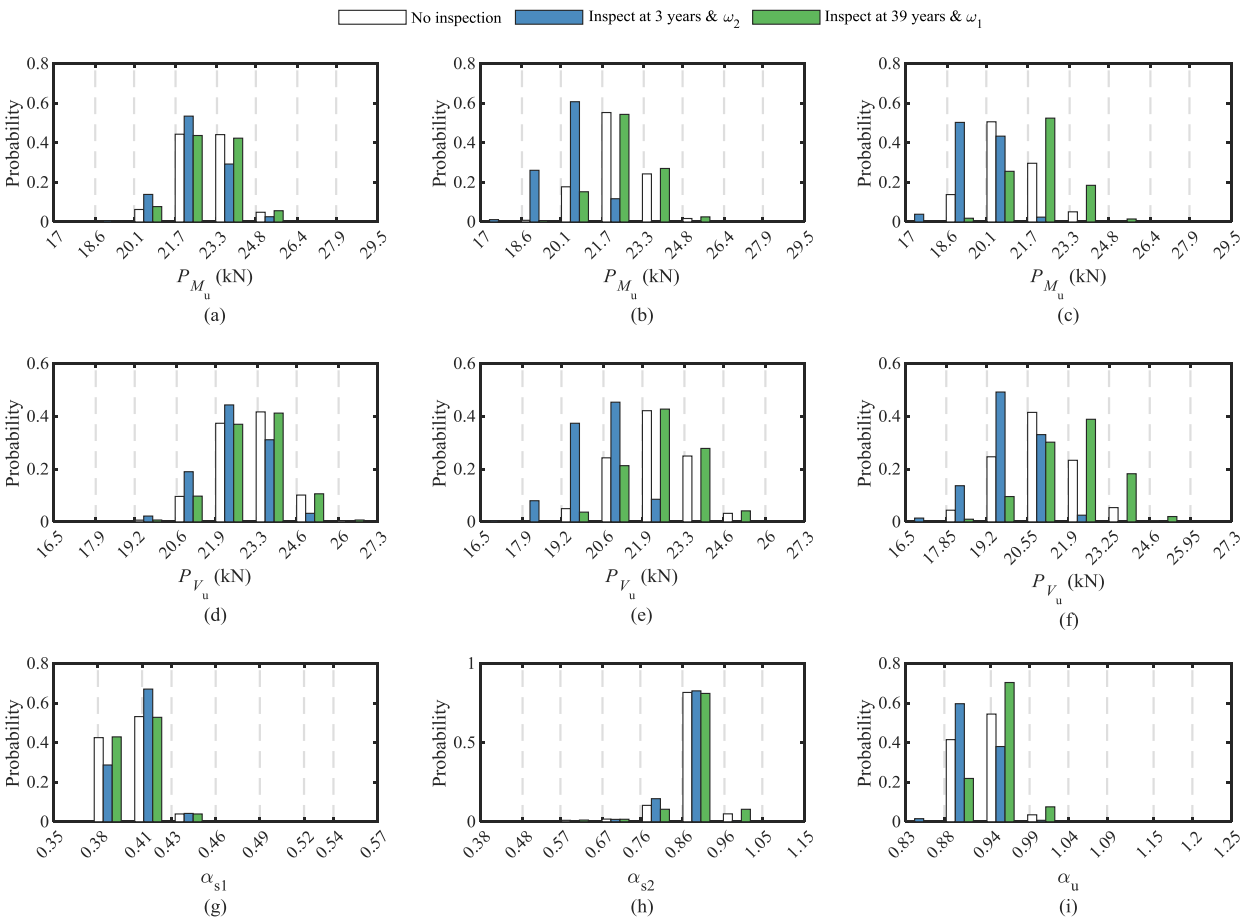

Fig. 9 PMFs of critical nodes in MBN: (a) P_{Mu} at 3 years; (b) P_{Mu} at 21 years; (c) P_{Mu} at 39 years; (d) P_{Vu} at 3 years; (e) P_{Vu} at 21 years; (f) P_{Vu} at 39 years; (g) α_{s1} at 3 years; (h) α_{s2} at 21 years; (i) α_{s3} at 39 years;

5.3.2. Effects of inspection results on mechanical capacities

This subsection investigates the influences of different inspection results on P_{Mu} and P_{Vu}. To facilitate the comparisons of different scenarios, the mean and standard deviation (STD) of discrete nodes are used here [2], which are calculated by Eqs. (39) and (40), respectively.

$$E(x) = 0.5 \cdot \sum_{k=1}^{n_x} \left(d_k + d_{k+1}\right) \cdot P_x(k) \tag{39}$$

$$\sqrt{D(x)} = \sqrt{\sum_{k=1}^{n_x} \left(0.5 \cdot \left(d_k + d_{k+1}\right) - E(x)\right)^2 \cdot P_x(k)} \tag{40}$$

in which x is the target node; $[d_1, d_2, \ldots, d_{n_x+1}]$ is the discretization scheme of x; and $P_x(k)$ is the PMF of x at its k-th interval.

Fig. 10 illustrates the mean and STD of P_{Mu} and P_{Vu} for different inspection results, where the mean value of P_{Mu} over time is higher than P_{Vu}, but the STD of P_{Mu} is lower than P_{Vu}. In Fig. 10a and b, the mean values keep decreasing with time, and those of P_{Mu} and P_{Vu} with the 3rd year inspection of ω_2 decrease the fastest among all scenarios, with maximum

reductions of 8.8% and 8.7% for P_{Mu} and P_{Vu} compared to no inspection. In addition, for the 21st-year inspection, the mean values of P_{Mu} and P_{Vu} decreased much more slowly than in other scenarios, with a maximum increase of 6.5% and 5.4% for P_{Mu} and P_{Vu} compared to no inspection. Moreover, compared to other years of inspection, P_{Mu} and P_{Vu} of the 39th-year inspection are closer to no inspection. The above results indicate that early inspection of moderate-width cracks significantly reduces the mean value of the load capacity. Also, small cracks observed at the middle to late service life dramatically increase the mean value of the load capacity because large cracks are expected after 21 years of exposure.

On the other hand, the STD of P_{Mu} and P_{Vu} (Fig. 10c and d) indicate that STD values initially increase and then decrease. The peak of STD depends on the inspection results. For instance, given the 21st-year inspection of ω_2, the STDs of P_{Mu} and P_{Vu} peak in 6 and 9 years, respectively, 4.8% and 0.64% higher than no inspection, while given that of ω_1, both the STDs of P_{Mu} and P_{Vu} peak in 51 years, 5.7% and 10.2% higher than no inspection. Such results indicate that, given the inspection time, the larger concrete crack could advance the STD peak of load capacity.

In addition, given the 3rd year inspection of ω_2, the STDs of P_{Mu} and P_{Vu} peak in 3 and 6 years, 3.7% higher and 1.3% lower than no inspection, while given the 39th year inspection of ω_2, both the STDs of P_{Mu} and P_{Vu} peak in 33 years, 5.1% and 1.1% lower than no inspection. Therefore, given the inspection results for concrete crack width, the earlier the inspection occurs, the earlier the STD of load capacity reaches its peak.

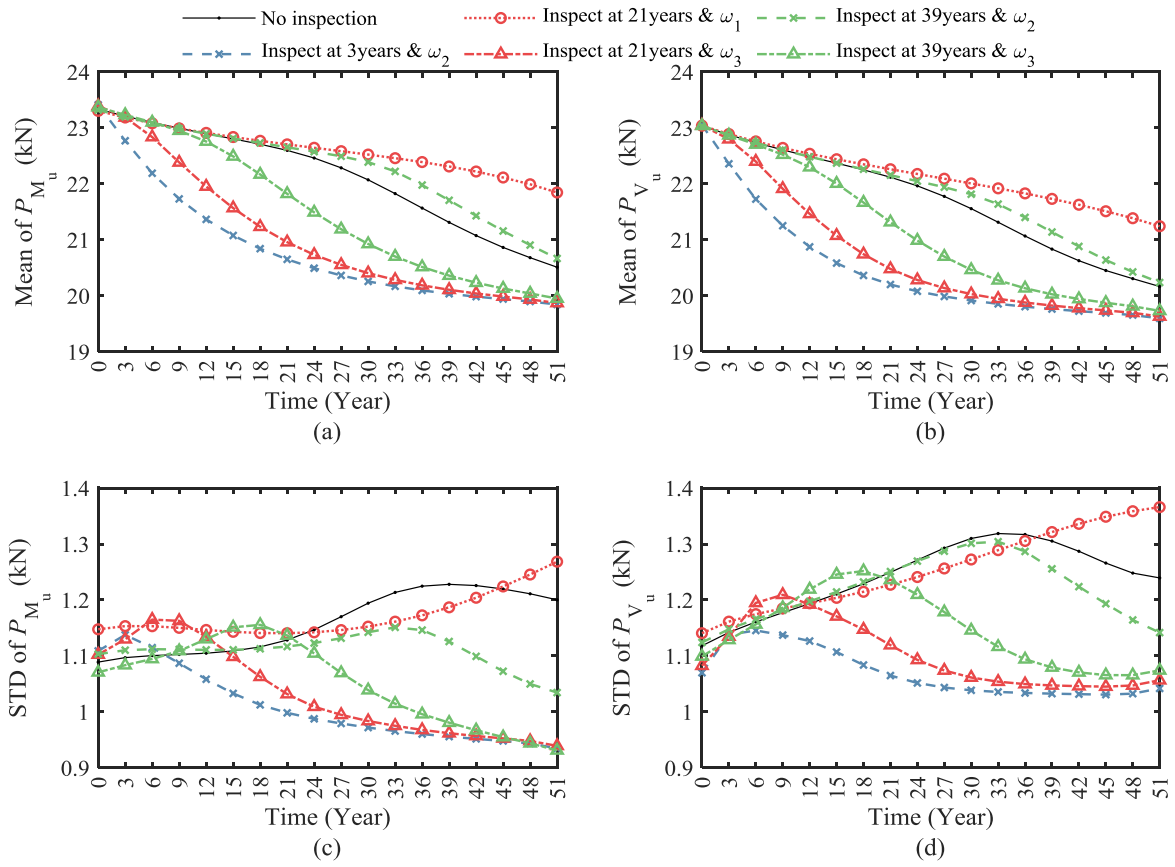

Fig. 10 Mean and STD of P_{Mu} and P_{Vu} subject to different inspection results: (a) Mean of P_{Mu};

(b) Mean of P_{Vu}; (c) STD of P_{Mu}; and (d) STD of P_{Vu}

5.3.3. Effects of inspection results on failure probabilities

This subsection investigates the influences of inspection results on failure probabilities considering different limit states, as illustrated in Fig. 11-Fig. 13. The effects of inspection on failure probabilities for SLS (p_{fs1} and p_{fs2}) are not as pronounced as those for the ULS (p_{fu}) in most scenarios. Consequently, only a few scenarios that demonstrate significant differences from the no inspection results are presented in Fig. 11 and Fig. 12. For SLS1 (Eq.(30) with 0.05 mm limit cracks size), $p_{f,s1}$ ranges from 0.65 to 1 for all scenarios. Meanwhile, Fig. 11 shows that the differences among different scenarios are limited and decrease rapidly over time until it is below 1% after 6 years. Among the displayed scenarios with inspection, the highest $p_{f,s1}$ could be found under the 3rd-year inspection of ω_2 5.2% higher than no inspection, followed by the 12th-year inspection of ω_3 (4.8% higher than no inspection) and the lowest in the 30th-year inspection of ω_3 (1.4% higher than no inspection). Such a result might suggest that the occurrence probability of a 0.05 mm loading crack is relatively high in this case and therefore $p_{f,s1}$ is not sensitive to the inspection results of corrosion-induced cracks.

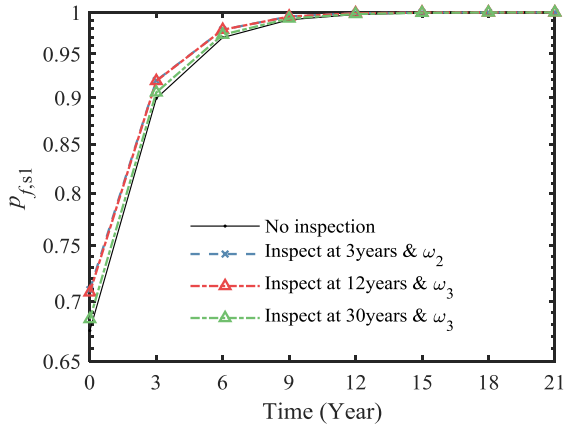

Fig. 11 Time-dependent failure probability $p_{f,\,s1}$ of the beam under SLS1 and different inspection results

Furthermore, for SLS2, Fig. 12 illustrates that given the inspection results of ω_2, $p_{f,s2}$ is ranging from 10^{-3} to 0.04, and $p_{f,s2}$ varies nonlinearly over time. For instance, given the 3rd-year and 12th-year inspection of ω_2, $p_{f,s2}$ is initially 12.7% and 5.1% higher, 30.2% and 11.8% lower but eventually 19.1% and 9.7% higher than no inspection, respectively. However, for the 30th-year inspection of ω_2, $p_{f,s2}$ is maximum 13.5% higher than no inspection before 45 years but 3.7% lower than no inspection until the end of service life. The above results indicate that the occurrence probability of a 1 mm loading crack is more sensitive to inspection results of corrosion-induced crack than that of a 0.05 mm loading crack. Besides, the influences of corrosion-induced cracks on 1 mm loading cracks appear of particular nonlinearity and hysteresis.

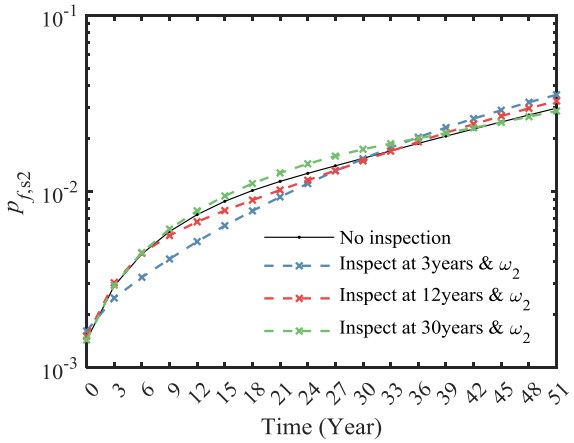

Fig. 12 Time-dependent failure probability $p_{f,\,s2}$ of the beam under SLS2 and different inspection results

On the other hand, for the ultimate limit state, Fig. 13 shows that $p_{f,u}$ for all scenarios ranges from 2×10^{-5} to 0.035 all over the service life, and the effects of inspection results on $p_{f,u}$ are dramatic. For instance, given the 3rd year inspection of ω_2 and 12th year inspecton of ω_3, $p_{f,u}$ is 506% and 530% higher than no inspection. Such a result demonstrates that a high width of corrosion-induced crack detected early in service life could significantly impair structural safety. In addition, given the inspections of crack width, $p_{f,u}$ decreases with the inspection time. For instance, $p_{f,u}$ with a 3rd-year inspection of ω_1 is maximum 8.2% lower than no inspection, and $p_{f,u}$ with a 30th-year inspection of ω_1 is maximum 63.8% lower than no inspection. Besides, $p_{f,u}$ with the 12th-year inspection of ω_2 is maximum 290% higher than no inspection, while $p_{f,u}$ with the 30th-year inspection of ω_2 is maximum 30.7% higher and 4.3% lower than no inspection after 51 and 21 years, respectively. Thus, a smaller width of corrosion-induced cracks detected when approaching the end of service life implies better structural reliability and safety.

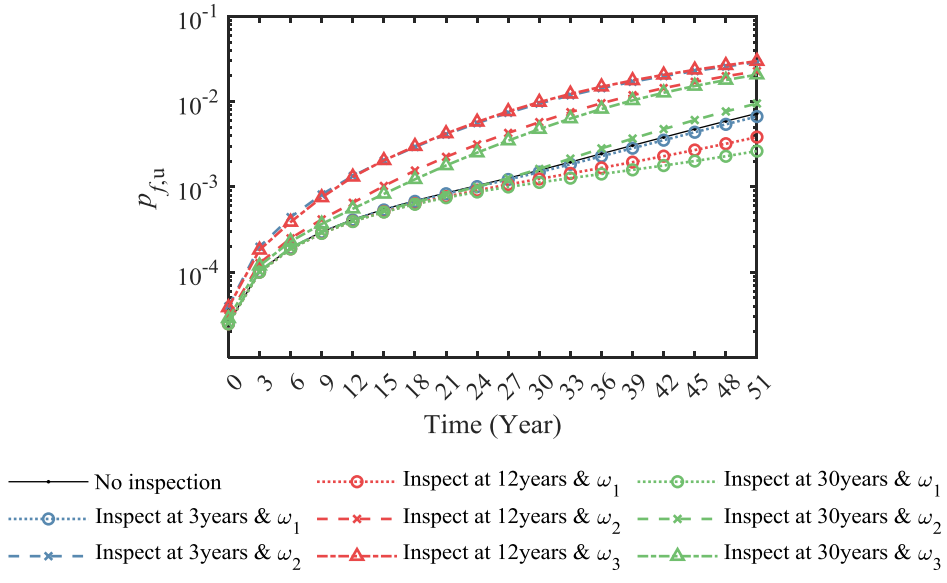

Fig. 13 Time-dependent failure probability $p_{f,u}$ of the beam considering on ULS and different inspection results

5.3.4. Effects of inspection results on failure modes

In this subsection, the inspection effects on failure modes are further investigated, as displayed in Fig. 14. Considering no inspection, the probability of shear failure after 3 years is basically the same as that of flexural failure and increases with time, exceeding that of flexural failure by 123.8% after 27 years. In addition, given the 12th and 30th-year inspection results of ω_1, the probabilities of flexural and shear failure initially do not change compared to no inspection (Fig. 14a). After 27 years, the probability of shear failure decreases by 7.4% and 25%, respectively, and that of flexural failure increases by 16.6% and 56.8%, respectively (Fig. 14b), compared to no inspection. Therefore, the later the inspection occurs, the higher the probability of flexural failure, given the inspection results of small crack widths.

Furthermore, given the 12th and 30th-year inspection results of ω_3, the probability of shear failure increases by 39.0% and 3.1% after 3 years, respectively, while the probability of flexural failure decreases by 42.6% and 3.4% after 3 years, compared to no inspection. Also, the probability of shear failure dramatically increases by 23.5% and 23.4% after 48 years, respectively, while the probability of flexural failure decreases by 81.6% and 81.3% after 48 years, compared to no inspection. Thus, inspection results for large crack widths lead to a significant increase in shear failure probability, which is advanced by when cracks are detected during the earlier inspection time.

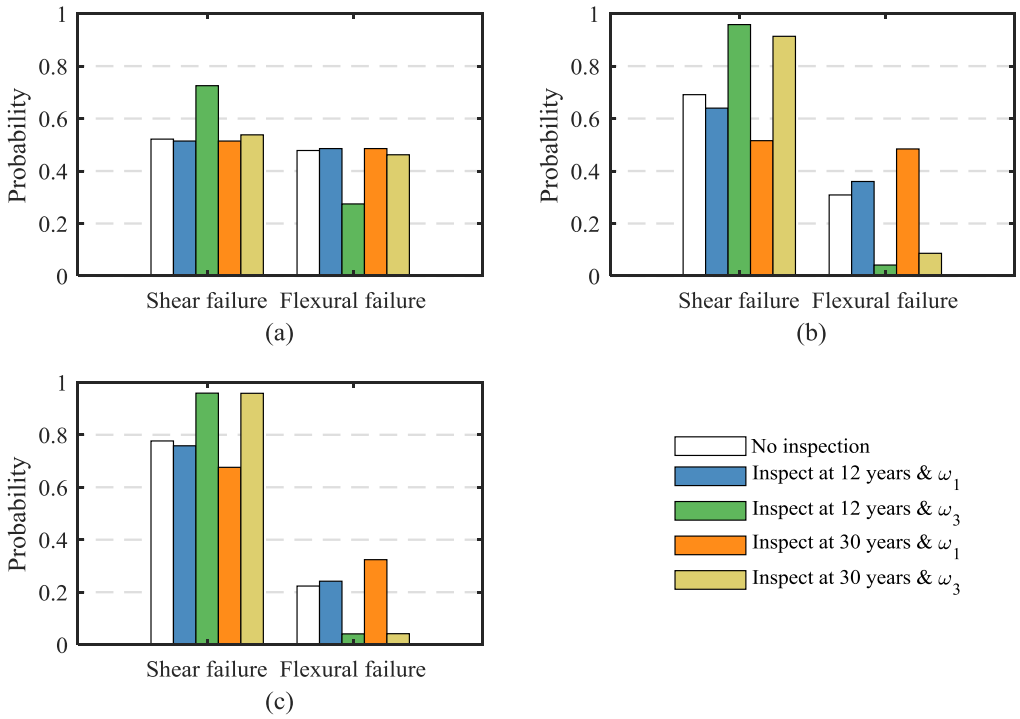

Fig. 14 Failure modes of the corroding RC beam subjected to different inspection results and time slices: (a) 3 years; (b) 27 years; and (c) 48 years

5.4.Other effects

In this section, the effects of other factors, e.g., exposure condition *ec*, and models of the environment and chloride transport on reliability estimation, are further discussed. For convenience, the probabilities of shear and flexural failure are directly compared. They are calculated by multiplying the failure probability of the corresponding limit states by the probability of failure mode over time, i.e., Eq.(41).

$$\begin{aligned} p_{f,M}(t) &= p_{f,u}(t) \cdot \Pr\left(F_{\mathrm{mod}}(t)=0|\mathrm{fail}\right), \\ p_{f,V}(t) &= p_{f,u}(t) \cdot \Pr\left(F_{\mathrm{mod}}(t)=1|\mathrm{fail}\right) \end{aligned} \tag{41}$$

where $\Pr(F_{\mathrm{mod}}(t)=0|\mathrm{fail})$ and $\Pr(F_{\mathrm{mod}}(t)=1|\mathrm{fail})$ are the probabilities of flexural and shear failure, respectively.

For exposure conditions, two *ec* (°C): $ec_1 \in [0, 0.6]$ and $ec_2 \in [2.9,3.5]$ are considered to study the low and high *ec*s and their effects on reliability estimation for no inspection and 21-th year inspection of ω_2, as illustrated in Fig. 15a and b. As shown, both the effects of inspection results and *ec* on $p_{\mathrm{f,M}}$ are nonlinear. The $p_{\mathrm{f,M}}$ with inspections firstly increases with time and then drops in 15 to 21 years but then rises in the rest of service life. Also, the $p_{\mathrm{f,M}}$ for given ec_1 and ec_2 gradually exceeds that of no given *ec*. Supposing the 21-th year inspection of ω_2 and given ec_1, the $p_{\mathrm{f,M}}$ is about 8.0% higher than no given *ec* at the end of service life, while given ec_2, $p_{\mathrm{f,M}}$ is about 27.3% higher at the end of service life. Thus, a higher *ec* results in higher growth in flexural failure probability near the end of service life.

In contrast to $p_{\mathrm{f,M}}$, considering no inspection, $p_{\mathrm{f,V}}$ with given ec_1 and ec_2 is about 1.0% to 13.2% lower than no given *ec* at most times. Meanwhile, considering the 21-th year inspection of ω_2 and no given *ec*, $p_{\mathrm{f,V}}$ is 2.4% to 175.6% higher than that without inspection. Such results suggest that inspection results might significantly affect shear failure probability more than *ec*.

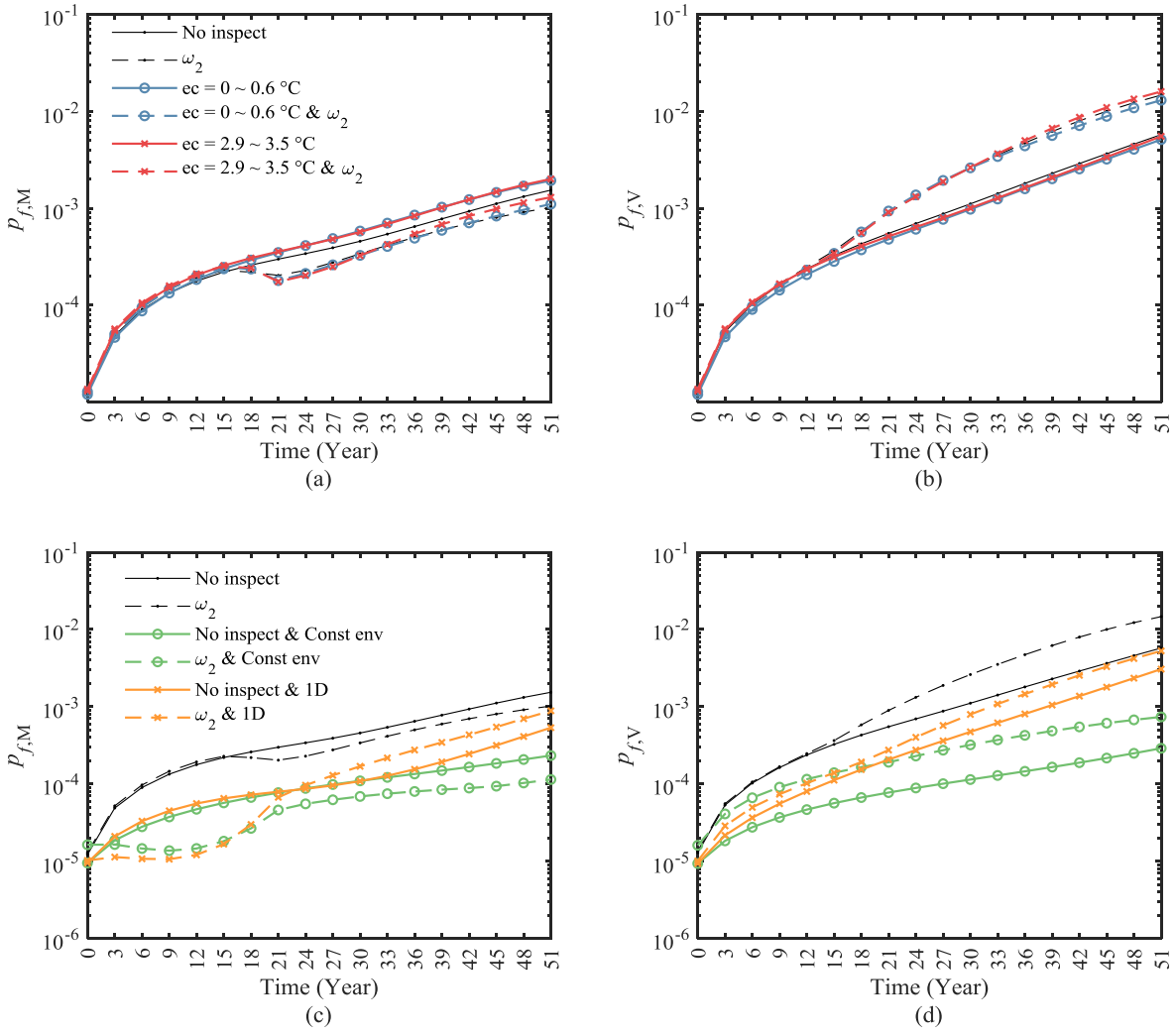

Fig. 15 Time-dependent probability of two failure modes subjected to different scenarios: (a) flexural failure probability & exposure conditions; (b) shear failure probability & exposure conditions;(c) flexural failure probability & environmental models &chloride transport modes; and (d) shear failure probability & environmental models & chloride transport modes

On the other hand, Fig. 15c and d present the $p_{f,M}$ and $p_{f,V}$ subject to constant environment and one-dimensional (1D) chloride transport. For 1D chloride transport, the $p_{f,M}$ with the 21-th year inspection of ω_2 is 65.5% higher at the end of service life, compared to no inspection. In addition, compared to 2D chloride transport, $p_{f,M}$ and $p_{f,V}$ without inspection is 21.9% to 76.4% lower, while the 21-th year inspection of ω_2 results in 13.3% to 93.7% decrease on $p_{f,M}$ and $p_{f,V}$. Thus, as illustrated in Fig. 15c and d, considering 1D chloride transport underestimates the failure probability drastically.

In addition, for the constant environment, $p_{f,M}$ and $p_{f,V}$ without inspection are about 22.2% to 95.0% lower while considering the 21-th year inspection of ω_2, $p_{f,M}$ and $p_{f,V}$ are about 88.8% and 94.9% lower at the end of service life, compared to the time-varying environment. Thus, it can be found that ignoring the time-varying environment could decrease the probabilities of shear and flexural failure. Therefore, it could be concluded that 2D chloride transport and the time-varying environment affect the effects of inspection results on failure probability

assessment.

6. Conclusions

This study developed an MBN-based framework for the reliability estimation of RC structures subject to long-term environmental effects. This framework consists of three modules: durability assessment, mechanical assessment, and reliability assessment, achieved by the combination of SBN and DBN. The information between adjacent BN is transferred by applying pinch points and soft evidence. The time-dependent reliability analysis for RC beams under marine atmospheric environment is made as one case to illustrate the effectiveness of the proposed framework, and the following conclusion can be drawn:

(1) Inference results of MBN prove that the proposed framework could use the results of inspections to update the probabilistic distribution of time-dependent mechanical capacity, FEM adjustment coefficients, and performance functions. The flexural and shear load capacity negatively correlate with the corrosion-induced crack width, while the FEM adjustment coefficient is nonlinearly related.

(2) For load capacities, results indicate that early inspection of medium-width cracks decreases the mean values of load capacities by about 9% while the small-width cracks raise the mean values of load capacities by about 5 to 6%. Also, the earlier inspection time and wider cracks could advance the peak of STD for load capacities.

(3) Failure probabilities subject to different limit states suggest that the effects of inspection on the failure probability of serviceability limit states are nonlinearly related to inspection results and not as significant as those of the ultimate limit state. Given the inspection of corrosion-induced cracks, compared to no inspection, the probability of a 0.05mm loading crack is about 1% to 5% higher, and that of a 1 mm loading crack is about 5% to 13% higher initially but then about 3% to 30% lower. Regarding ultimate limit states and the assumed conditions in the case study, an early inspection of large corrosion-induced cracks might dramatically overestimate the failure probability by about 500%, and later inspection of small corrosion-induced cracks might underestimate the failure probability by about 64%.

(4) Failure mode analysis gives that the probabilities of shear failure and flexural failure are positively and negatively correlated with the inspection results, respectively. Results show that a later inspection result of small corrosion-induced cracks might increase the probability of flexural failure mode by about 16% to 57% and decrease that of shear failure mode by about 7% to 25%. In addition, large corrosion-induced cracks significantly increase the probability of shear failure mode by 3% to 39% and decrease that of flexural failure mode by about 3% to 81%.

(5) Sensitivity analysis results show that the effects of exposure conditions on the failure probability of different failure modes are different and nonlinear. Given the small characteristics value of exposure condition ec_1, compared to no given ec, the failure probability of flexural failure could increase by 3.6% to 32%, while that of shear failure could reduce by about 2% to 12%. Given a large characteristic value of exposure condition ec_2, the failure probability of flexural failure could increase by 7.2% to 33%, while that of shear failure could increase by 1.6% to 10%. Moreover, considering the

constant environment and one-dimensional chloride transport could significantly reduce the failure probabilities of shear and flexural failure by about 13 to 94% and 22% to 95%, respectively. Thus, ignoring the effects of the time-varying environment and two-dimensional chloride transport underestimate the failure probability and overestimate the effects of inspection results on failure probability at the early stage.

In summary, it is practical to use the proposed MBN framework for the reliability assessment of RC structures developed. The proposed approach can integrate the inspection data with the life-cycle design and management of RC infrastructure and dramatically mitigate the uncertainty in the life-cycle assessment of corroding RC structures. In future studies, it is significant to take into account the impact of spatial correlation of stochastic parameters in concrete durability assessment. Furthermore, it is critical to incorporate spatial variations in corrosion-induced crack by integrating random field theory and mesoscale multi-physics field modeling. Besides, various inspection techniques, such as half-cell potential method, Linear Sweep Voltammetry (LSV), need to be investigated to further enhance the MBN based reliability assessment of RC structures subject to marine atmospheric environments in future research. The above efforts will contribute to advancing the knowledge and applicability of our findings in real-world scenarios.

References:

[1] Guo HY, Dong Y, Gu XL. Durability assessment of reinforced concrete structures considering global warming: A performance-based engineering and experimental approach. Constr Build Mater 2020;233:117251. https://doi.org/10.1016/j.conbuildmat.2019.117251.

[2] Guo HY, Dong Y. Dynamic Bayesian network for durability of reinforced concrete structures in long-term environmental exposures. Eng Fail Anal 2022;142:106821. https://doi.org/10.1016/j.engfailanal.2022.106821.

[3] Qu F, Li W, Dong W, Tam VWY, Yu T. Durability deterioration of concrete under marine environment from material to structure: A critical review. J Build Eng 2021;35:102074. https://doi.org/10.1016/j.jobe.2020.102074.

[4] ASCE. ASCE's 2021 Infrastructure Report Card 2021:18–25.

[5] Crummey E, Afroz S, Park J, Rhodes N. Costing Climate Change Impacts to Public Infrastructure Assessing the financial impacts of extreme rainfall, extreme heat, and freeze-thaw cycles on public buildings in Ontario. 2022 ICEAA Conf., 2022.

[6] Ahmad S. Reinforcement corrosion in concrete structures, its monitoring and service life prediction - A review. Cem Concr Compos 2003;25:459–71. https://doi.org/10.1016/S0958-9465(02)00086-0.

[7] Frangopol DM, Lin K-Y, Estes AC. Reliability of reinforced concrete girders under corrosion attack. J Struct Eng 1997;123:286–97. https://doi.org/10.1061/(asce)0733-9445(1997)123:3(286).

[8] Stewart MG, Suo Q. Extent of spatially variable corrosion damage as an indicator of strength and time-dependent reliability of RC beams. Eng Struct 2009;31:198–207. https://doi.org/10.1016/j.engstruct.2008.08.011.

[9] Stewart MG. Spatial variability of pitting corrosion and its influence on structural

fragility and reliability of RC beams in flexure. Struct Saf 2004;26:453–70. https://doi.org/10.1016/j.strusafe.2004.03.002.
[10] Stewart MG, Al-Harthy A. Pitting corrosion and structural reliability of corroding RC structures: Experimental data and probabilistic analysis. Reliab Eng Syst Saf 2008;93:373–82. https://doi.org/10.1016/j.ress.2006.12.013.
[11] Stewart MG. Mechanical behaviour of pitting corrosion of flexural and shear reinforcement and its effect on structural reliability of corroding RC beams. Struct Saf 2009;31:19–30. https://doi.org/10.1016/j.strusafe.2007.12.001.
[12] Val D V. Deterioration of strength of RC beams due to corrosion and its influence on beam reliability. J Struct Eng 2007;133:1297–306. https://doi.org/10.1061/(ASCE)0733-9445(2007)133:9(1297).
[13] Guo HY, Dong Y, Gu XL. Two-step translation method for time-dependent reliability of structures subject to both continuous deterioration and sudden events. Eng Struct 2020;225:111291. https://doi.org/10.1016/j.engstruct.2020.111291.
[14] Bastidas-Arteaga E, Schoefs F, Stewart MG, Wang X. Influence of global warming on durability of corroding RC structures: A probabilistic approach. Eng Struct 2013;51:259–66. https://doi.org/10.1016/j.engstruct.2013.01.006.
[15] Zacchei E, Bastidas-Arteaga E. Multifactorial Chloride Ingress Model for Reinforced Concrete Structures Subjected to Unsaturated Conditions. Buildings 2022;12. https://doi.org/10.3390/buildings12020107.
[16] Zhang MY, Song HJ, Lim S, Akiyama M, Frangopol DM. Reliability estimation of corroded RC structures based on spatial variability using experimental evidence, probabilistic analysis and finite element method. Eng Struct 2019;192:30–52. https://doi.org/10.1016/j.engstruct.2019.04.085.
[17] Guo HY, Dong Y, Bastidas-Arteaga E, Gu XL. Probabilistic failure analysis, performance assessment, and sensitivity analysis of corroded reinforced concrete structures. Eng Fail Anal 2021;124:105328. https://doi.org/10.1016/j.engfailanal.2021.105328.
[18] Estes AC, Frangopol DM. Updating Bridge Reliability Based on Bridge Management Systems Visual Inspection Results. J Bridg Eng 2003;8:374–82. https://doi.org/10.1061/(asce)1084-0702(2003)8:6(374).
[19] Straub D, Der Kiureghian A. Bayesian Network Enhanced with Structural Reliability Methods: Application. J Eng Mech 2010;136:1259–70. https://doi.org/10.1061/(asce)em.1943-7889.0000170.
[20] Straub D, Der Kiureghian A. Bayesian Network Enhanced with Structural Reliability Methods: Methodology. J Eng Mech 2010;136:1248–58. https://doi.org/10.1061/(asce)em.1943-7889.0000173.
[21] Tesfamariam S, Martín-Pérez B. Bayesian Belief Network to Assess Carbonation-Induced Corrosion in Reinforced Concrete. J Mater Civ Eng 2008;20:707–17. https://doi.org/10.1061/(asce)0899-1561(2008)20:11(707).
[22] Deby F, Carcasses M, Sellier A. Toward a probabilistic design of reinforced concrete durability: Application to a marine environment. Mater Struct Constr 2009;42:1379–91. https://doi.org/10.1617/s11527-008-9457-8.

[23] Deby F, Carcasses M, Sellier A. Simplified models for the engineering of concrete formulations in a marine environment through a probabilistic method. Eur J Environ Civ Eng 2012;16:362–74. https://doi.org/10.1080/19648189.2012.667716.
[24] Tran TB, Bastidas-Arteaga E, Schoefs F. Improved Bayesian network configurations for probabilistic identification of degradation mechanisms: application to chloride ingress. Struct Infrastruct Eng 2016;12:1162–76. https://doi.org/10.1080/15732479.2015.1086387.
[25] Tran TB, Bastidas-Arteaga E, Schoefs F. Improved Bayesian network configurations for random variable identification of concrete chlorination models. Mater Struct Constr 2016;49:4705–18. https://doi.org/10.1617/s11527-016-0818-4.
[26] Tran TB, Bastidas-Arteaga E, Schoefs F, Bonnet S. A Bayesian network framework for statistical characterisation of model parameters from accelerated tests: application to chloride ingress into concrete. Struct Infrastruct Eng 2018;14:580–93. https://doi.org/10.1080/15732479.2017.1377737.
[27] Tran TB, Bastidas-Arteaga E, Aoues Y. A Dynamic Bayesian Network framework for spatial deterioration modelling and reliability updating of timber structures subjected to decay. Eng Struct 2020;209:110301. https://doi.org/10.1016/j.engstruct.2020.110301.
[28] Murphy KP. Dynamic Bayesian Networks: Representation, Inference and Learning. University of California, Berkeley, 2002.
[29] Ma Y, Wang L, Zhang J, Xiang Y, Liu Y. Bridge Remaining Strength Prediction Integrated with Bayesian Network and In Situ Load Testing. J Bridg Eng 2014;19:04014037. https://doi.org/10.1061/(asce)be.1943-5592.0000611.
[30] Hackl J, Kohler J. Reliability assessment of deteriorating reinforced concrete structures by representing the coupled effect of corrosion initiation and progression by Bayesian networks. Struct Saf 2016;62:12–23. https://doi.org/10.1016/j.strusafe.2016.05.005.
[31] Val D V., Trapper PA. Probabilistic evaluation of initiation time of chloride-induced corrosion. Reliab Eng Syst Saf 2008;93:364–72. https://doi.org/10.1016/j.ress.2006.12.010.
[32] Bastidas-Arteaga E, Chateauneuf A, Sánchez-Silva M, Bressolette P, Schoefs F. A comprehensive probabilistic model of chloride ingress in unsaturated concrete. Eng Struct 2011;33:720–30. https://doi.org/10.1016/j.engstruct.2010.11.008.
[33] Bastidas-Arteaga E. Reliability of Reinforced Concrete Structures Subjected to Corrosion-Fatigue and Climate Change. Int J Concr Struct Mater 2018;12. https://doi.org/10.1186/s40069-018-0235-x.
[34] Bensi M, Der Kiureghian A, Straub D. Bayesian network modeling of correlated random variables drawn from a Gaussian random field. Struct Saf 2011;33:317–32. https://doi.org/10.1016/j.strusafe.2011.05.001.
[35] Zhou BB, Gu XL, Guo HY, Zhang WP, Huang QH. Polarization behavior of activated reinforcing steel bars in concrete under chloride environments. Constr Build Mater 2018;164:877–87. https://doi.org/10.1016/j.conbuildmat.2018.01.187.
[36] Li Q, Ye X. Surface deterioration analysis for probabilistic durability design of RC structures in marine environment. Struct Saf 2018;75:13–23. https://doi.org/10.1016/j.strusafe.2018.05.007.

[37] Yi G, Ye X, Li Q. Empirical Study of Surface Deterioration Analysis Based on Random Fields for Reinforced Concrete Structures in Marine Environment. Materials (Basel) 2023;16. https://doi.org/10.3390/ma16114150.
[38] Guo HY, Jiang C, Gu XL, Dong Y, Zhang WP. Time-dependent reliability analysis of reinforced concrete beams considering marine environmental actions. Eng Struct 2023;288:116252. https://doi.org/10.1016/j.engstruct.2023.116252.
[39] Flint MM, Baker JW, Billington SL. A modular framework for performance-based durability engineering: From exposure to impacts. Struct Saf 2014;50:78–93. https://doi.org/10.1016/j.strusafe.2014.03.003.
[40] Yu Y, Chen X, Gao W, Wu D, Castel A. Impact of atmospheric marine environment on cementitious materials. Corros Sci 2019;148:366–78. https://doi.org/10.1016/j.corsci.2018.12.021.
[41] Bastidas-Arteaga E, Chateauneuf A, Sánchez-Silva M, Bressolette P, Schoefs F. Influence of weather and global warming in chloride ingress into concrete: A stochastic approach. Struct Saf 2010;32:238–49. https://doi.org/10.1016/j.strusafe.2010.03.002.
[42] Saetta A V, Schrefler BA, Vitaliani R V. The carbonation of concrete and the mechanism of moisture, heat and carbon dioxide flow through porous materials. Cem Concr Res 1993;23:761–72.
[43] Carnahan B, Luther HA. Applied numerical methods. New York: John Wiley & Sons; 1969.
[44] Liu T, Weyers RW. Modeling the dynamic corrosion process in chloride contaminated concrete structures. Cem Concr Res 1998;28:365–79. https://doi.org/10.1016/S0008-8846(98)00259-2.
[45] Vidal T, Castel A, François R. Analyzing crack width to predict corrosion in reinforced concrete. Cem Concr Res 2004;34:165–74. https://doi.org/10.1016/S0008-8846(03)00246-1.
[46] González JA, Andrade C, Alonso C, Feliu S. Comparison of rates of general corrosion and maximum pitting penetration on concrete embedded steel reinforcement. Cem Concr Res 1995;25:257–64. https://doi.org/10.1016/0008-8846(95)00006-2.
[47] Kwon SJ, Na UJ, Park SS, Jung SH, Jun S, Jin U, et al. Service life prediction of concrete wharves with early-aged crack: Probabilistic approach for chloride diffusion. Struct Saf 2009;31:75–83. https://doi.org/10.1016/j.strusafe.2008.03.004.
[48] Bazant ZP, Sener S, Kim JK. Effect of Cracking on Drying Permeability and Diffusivity of Concrete. ACI Mater J 1987;84:351–7. https://doi.org/10.14359/1739.
[49] Gu XL, Guo HY, Zhou B Bin, Zhang WP, Jiang C. Corrosion non-uniformity of steel bars and reliability of corroded RC beams. Eng Struct 2018;167:188–202. https://doi.org/10.1016/j.engstruct.2018.04.020.
[50] Zhao YX, Karimi AR, Wong HS, Hu BY, Buenfeld NR, Jin WL. Comparison of uniform and non-uniform corrosion induced damage in reinforced concrete based on a Gaussian description of the corrosion layer. Corros Sci 2011;53:2803–14. https://doi.org/10.1016/j.corsci.2011.05.017.
[51] Kashani MM, Crewe AJ, Alexander NA. Use of a 3D optical measurement technique for stochastic corrosion pattern analysis of reinforcing bars subjected to accelerated

corrosion. Corros Sci 2013;73:208–21. https://doi.org/10.1016/j.corsci.2013.03.037.
[52] Vecchio FJ, Collins MP. The modified compression-field theory for reinforced concrete elements subjected to shear. ACI J Proc 1986;83:219–31. https://doi.org/10.14359/10416.
[53] Horidijk DA. Local approach to fatigue of concrete (PhD Thesis). Delft University of Technology, The Netherlands, 1991.
[54] Feenstra PH. Computational aspects of biaxial stress in plain and reinforced concrete (PhD Thesis). Delft University of Technology, The Netherlands, 1993.
[55] Zeng YH, Gu XL, Zhang WP, Huang QH. Study on mechanical properties of corroded prestressed tendons. Jianzhu Cailiao Xuebao/Journal Build Mater 2010;13:169–74. https://doi.org/10.3969/j.issn.1007-9629.2010.02.008.
[56] Almusallam AA. Effect of degree of corrosion on the properties of reinforcing steel bars. Constr Build Mater 2001;15:361–8. https://doi.org/10.1016/S0950-0618(01)00009-5.
[57] Palsson R, Mirza MS. Mechanical response of corroded steel reinforcement of abandoned concrete bridge. ACI Struct J 2002;99:157–62. https://doi.org/10.14359/11538.
[58] Zhang WP, Shang DF, Gu XL. Stress-Strain relationship of corroded steel bars. J Tongji Univ Sci 2006;5:586 (In Chinese).
[59] Zhang WP, Song X Bin, Gu XL, Li S Bin. Tensile and fatigue behavior of corroded rebars. Constr Build Mater 2012;34:409–17. https://doi.org/10.1016/j.conbuildmat.2012.02.071.
[60] Apostolopoulos CA, Papadopoulos MP. Tensile and low cycle fatigue behavior of corroded reinforcing steel bars S400. Constr Build Mater 2007;21:855–64. https://doi.org/10.1016/j.conbuildmat.2005.12.012.
[61] Zhang WP, Chen H, Gu XL. Tensile behaviour of corroded steel bars under different strain rates. Mag Concr Res 2016;68:127–40. https://doi.org/10.1680/jmacr.15.00174.
[62] Kallias AN, Imran Rafiq M. Finite element investigation of the structural response of corroded RC beams. Eng Struct 2010;32:2984–94. https://doi.org/10.1016/j.engstruct.2010.05.017.
[63] El Maaddawy T, Soudki K, Topper T, Bischoff PH. Analytical model to predict nonlinear flexural behavior of corroded reinforced concrete beams. ACI Struct J 2006;103:469–72.
[64] Maaddawy E, Soudki K, Topper T. Analytical model to predict non-linear flexural behavior of corroded reinforced concrete beams. ACI Struct J 2005;4:550–9.
[65] Šavija B, Luković M, Pacheco J, Schlangen E. Cracking of the concrete cover due to reinforcement corrosion: A two-dimensional lattice model study. Constr Build Mater 2013;44:626–38. https://doi.org/10.1016/j.conbuildmat.2013.03.063.
[66] Stewart MG, Wang X, Nguyen MN. Climate change impact and risks of concrete infrastructure deterioration. Eng Struct 2011;33:1326–37. https://doi.org/10.1016/j.engstruct.2011.01.010.
[67] Ma Y, Zhang J, Wang L, Liu Y. Probabilistic prediction with bayesian updating for strength degradation of RC bridge beams. Struct Saf 2013;44:102–9.

https://doi.org/10.1016/j.strusafe.2013.07.006.
[68] Nagarajan R, Scutari M, Lèbre S. Bayesian Networks in R. 2013. https://doi.org/10.1007/978-1-4614-6446-4.
[69] Scutari M, Denis J-B. Bayesian Networks with examples in R. 2014. https://doi.org/10.1201/b17065.
[70] Zhang HF, Zhang WP, Gu XL, Jin XY, Jin NG. Chloride penetration in concrete under marine atmospheric environment – analysis of the influencing factors. Struct Infrastruct Eng 2016;12:1428–38. https://doi.org/10.1080/15732479.2015.1134588.
[71] Val D V., Melchers RE. Reliability of deteriorating RC slab bridges. J Struct Eng 1997;123:1638–44. https://doi.org/10.1061/(ASCE)0733-9445(1997)123:12(1638).
[72] Tu B, Dong Y, Fang Z. Time-Dependent Reliability and Redundancy of Corroded Prestressed Concrete Bridges at Material, Component, and System Levels. J Bridg Eng 2019;24. https://doi.org/10.1061/(asce)be.1943-5592.0001461.
[73] Darmawan MS, Stewart MG. Spatial time-dependent reliability analysis of corroding pretensioned prestressed concrete bridge girders. Struct Saf 2007;29:16–31. https://doi.org/10.1016/j.strusafe.2005.11.002.
[74] Ye ZW, Zhang WP, Gu XL. Deterioration of shear behavior of corroded reinforced concrete beams. Eng Struct 2018;168:708–20. https://doi.org/10.1016/j.engstruct.2018.05.023.
[75] Guo HY, Dong Y, Gardoni P. Efficient subset simulation for rare-event integrating point-evolution kernel density and adaptive polynomial chaos kriging. Mech Syst Signal Process 2022;169:108762. https://doi.org/10.1016/j.ymssp.2021.108762.
[76] Hajializadeh D, Stewart MG, Enright B, O'Brien EJ. Spatial time-dependent reliability analysis of reinforced concrete slab bridges subject to realistic traffic loading. Struct Infrastruct Eng 2015:1–16. https://doi.org/10.1080/15732479.2015.1086385.
[77] Zwirglmaier K, Straub D. A discretization procedure for rare events in Bayesian networks. Reliab Eng Syst Saf 2016;153:96–109. https://doi.org/10.1016/j.ress.2016.04.008.

Appendix:

A1. Algorithms of Node discretization and CPT computation

The node discretization and CPT computation are implemented based on the methods from [2]. Taking a DBN with a set of nodes $X_{1:n_{bn}}^{i}=\{X_1^i, X_2^i,\ldots, X_{n_{bn}}^{i}\}$ ($i=1,2,\ldots, T$) as one example, the procedures of node discretization are presented. For DBN, the node discretization of all nodes remains unchanged over time slices. Thus, the corresponding discretization scheme of each node X_j (j = 1,…,n_{bn}) could be represented as D_{Xj} = [d_1, d_2,…, $d_{m_{Xj}+1}$] with m_{X_j} equal intervals.

For those isolated parent nodes (time-independent parent nodes) given the distribution types and parameters (such as the variables in Table 2), their lower and upper bounds (d_1 and $d_{m_{Xj}+1}$) could be preset, and their PMFs can be expressed by [77]:

$$P_{X_j}(k)=F_{X_j}(d_{k+1})-F_{X_j}(d_k),\ k=1,\ldots,m_{X_j} \tag{42}$$

where $F_{X_j}(\cdot)$ denotes the CDF of X_j.

For other types of nodes (child nodes or time-dependent parent nodes) without preset distribution functions, their lower d_1 and upper bounds $d_{m_{Xj}+1}$ can be determined by the minimum and maximum values of these nodes in the N number of representative samples [2]. It is essential to note that in MBN, although the CPTs of the pinch point variables are different in the adjacent sub-BNs, their discretization schemes must be consistent for soft evidence transfer and update.

Furthermore, the CPT of other types of nodes comes from the joint distribution of investigated nodes and their parent nodes. For the sake of expression, other types of nodes are noted as $Z_{1:n_c}^{i}=\left\{Z_1^i, Z_2^i,\ldots, Z_{n_c}^{i}\right\}$ (n_c is the number of nodes, and their CPT could be computed through the following steps:

(1) The discrete number of Z_j^i is noted as m_{Z_j}, and parent nodes are marked as a collection set $X_{col}=\left[X_b^i,\ldots, X_e^i\right]$ (b and e denote the serial numbers of the parent nodes in topological order from the beginning to the end of the sequence). For the first representative sample and the first time slice, let k = 1 and i = 1. For other time slices, the Z_j^{i-1} is becomes the first parent node of Z_j^i and X_{col} is revised as $\left[Z_j^{i-1}, X_b^i,\ldots, X_e^i\right]$;

(2) Determine the state z_j^i of the k-th sample and the i-th time slice of Z_j^i (denoted as $Z_{j,k}^{[i]}$) based on its discretization scheme D_{Zj};

(3) Determine the states of all parent nodes in topological order and store these states as $\boldsymbol{x}_{pa}$=

$[x_{pa,b},\ldots.x_{pa,e}]$ for the first time slice and $[z^{i-1}_j,\ x_{pa,b},\ldots.x_{pa,e}]$ for other time slices. Meanwhile, calculate a state variable x_{temp} by Eq. (43);

$$x_{temp} = \begin{cases} x_{pa,b} + \sum_{p=b+1}^{e} \left(x_{pa,p} - 1\right) \cdot \prod_{o=b}^{p-1} m_{X_o}, i = 1 \\ z_j^{i-1} + \left(x_{pa,b} - 1\right) \cdot m_{Z_j} + \sum_{p=b+1}^{e} \left(x_{pa,p} - 1\right) \cdot m_{Z_j} \prod_{o=b}^{p-1} m_{X_o}, i > 1 \end{cases} \tag{43}$$

(4) Then, the value of the x_{temp}-th row and z^i_j -th column of CPT will be incremented by $p_{a,k}$, i.e., Eq. (44);

$$CPT\left(x_{temp}, z_j^i\right) = CPT\left(x_{temp}, z_j^i\right) + p_{a,k} \tag{44}$$

(5) For the CPT of the first time slice, if $k < N$, let $k=k+1$, and repeat step (2). For the CPT of other time slices, if $i < T$, let $i = i+1$, and repeat step (2); and

(6) Once step (5) stops, the final CPT should be normalized.

More details on the above computational algorithms refer to [2].